Department of Precision and Microsystems Engineering

Experimental dynamic substructuring using direct time-domain deconvolved impulse response functions

T. van der Horst

Report no	:	EM 2014.001
Coaches	:	ir. P.L.C. van der Valk and ir. M.V. van der Seijs
Professor	:	prof. dr. ir. A. van Keulen
Specialisation	:	Engineering Mechanics
Type of report	:	MSc. thesis
Date	:	February 14, 2014

TU Delft Delft University of Technology

Abstract

The dynamics of systems can be analysed by combining the dynamics of its components. This method is generally known as dynamic substructuring. It allows for efficient computation of the dynamics of structures that would otherwise be to complex to determine. Most dynamic substructuring approaches use the frequency domain for the re-assembling of the subcomponents. Recently, a different implementation of the dynamic substructuring method has been introduced: impulse based substructuring (IBS). It uses impulse response function in the time-domain for representing the dynamics of the subcomponents, obtained by numerical models or experimental testing. Compared to the frequency domain methods, the impulse based substructuring scheme proves to be advantageous when analysing the high-frequency characteristics of a system. The high-frequency dynamics are excited when the system is subjected to blasts, shocks or impulsive loading. Due to the sensitivity of the impulse based substructure scheme, experimentally obtained impulse response functions can not be used for describing the dynamics of a subsystem.

The focus of this thesis is developing a direct time-domain technique for determining the experimental impulse response. This is realised by introducing the inverse finite impulse response force filter, which operates independent of the output system response. This time-domain approach will avoid frequency domain induced errors, i.e. windowing, anti-aliasing and Fourier transforms, in the effort of determining a highly accurate impulse response functions. The quality of the time-domain acquired impulse response, as well as the measurement induced errors are tested on the impulse based substructuring scheme. The procedures are illustrated by application to an one-dimensional bar.

The inverse force filter is successful in finding the experimental (averaged) impulse response. The accuracy of the filter depends on the length of the filter and the conditioning of the force auto correlation matrix. The eigenvalue decomposition of this matrix led to the formulation of a selection criteria between replicate measurements and a filtering operation. The inverse filter can also be defined by using a Fourier transform and its inverse. If both methods are compared, it is shown that the time-domain approach is less accurate and time efficient.

The direct time-domain approach did not change the impulse response in such an extend that coupling by the impulse based substructuring scheme was possible. Since coupling between numerically simulated data is possible, measurement errors are introduced on the impulse response functions to test their sensitivity to the IBS scheme. It is observed that a small error on the exponential decay, of the perfect impulse response, directly resulted in uncoupled full system responses. This led to the identification of the modal parameters of the measurement to get rid of these amplitude errors, by means of the least squares complex exponential method. The perfect synthesised impulse response are successful in finding a coupled full system response.

Experimental dynamic substructuring only finds the full coupled response if a clean synthesised impulse response function of the subcomponents is used. It can also be concluded that the inverse filter is not as accurate as its frequency domain counterpart. However, the inverse force filter will make deconvolution of small parts of the output response possible. This is desirable when testing lightly damped structures.

Contents

Notation

Symbols

General meaning of often used symbols, unless otherwise noted in context:

$\boldsymbol{B}$	Signed Boolean assembly matrix	L	Length of subsystem
$\boldsymbol{C}$	Damping matrix	M	Sample length input
d	Diameter	$\boldsymbol{M}$	Mass matrix
E	Young's modulus	N	Sample length output
$\boldsymbol{f}$	Force filter array	Q	Sample length impulse response
$\boldsymbol{f}^{inv}$	Inverse force filter	$\boldsymbol{r}$	Auto-correlation
$\boldsymbol{F}$	Force filter Toeplitz matrix	$\boldsymbol{R}$	Auto-correlation matrix
$\boldsymbol{F}^{inv}$	Pseudo inverse Force Toeplitz matrix	$\boldsymbol{S}$	Time stepping matrix
$\mathcal{F}$	Fourier transform	t	Time
$\boldsymbol{g}$	Connection force array	$\boldsymbol{u}$	Output displacement field
$\boldsymbol{G}$	Spectral density matrix	$\boldsymbol{V}$	Eigenvector matrix
$\boldsymbol{h}$	Impulse response array	$\boldsymbol{x}$	Vibration mode
$\boldsymbol{H}$	Impulse response matrix	$\ast$	Convolution
$\boldsymbol{K}$	Stiffness matrix	$\star$	Correlation

Greek symbols:

β,γ	Newmark time integration parameters	μ	Modal mass
$\boldsymbol{\delta}$	Unit Impulse	ρ	Density
Δ	Step increment	ω	Circular frequency or eigenfrequency
ϵ	Amplitude error	ω_d	Damped eigenfrequency
$\boldsymbol{\lambda}$	Lagrange multipliers	ζ	Damping ratio
$\boldsymbol{\Lambda}$	Eigenvalue matrix		

Subscripts and superscripts:

$\hat{\bullet}$	Averaged matrix	$\dot{\bullet}$	First time derivative
$\overline{\bullet}$	Complex conjugate	$\tilde{\bullet}$	Prediction array
$\bullet^{(s)}$	Component of substructure s	$\bullet^{\dagger}$	Pseudo inverse of matrix
$\bullet_x$	DoF at position x	$\ddot{\bullet}$	Second time derivative

Abbreviations

DFT	Discrete Fourier transform	FRF	Frequency response function
DoF	Degrees of freedom	IDFT	Inverse discrete Fourier transform
FIR	Finite impulse response	IRF	Impulse response function

Chapter 1

Introduction

1.1 Research context

The modern engineer is faced with structures that are becoming lighter and increasingly more complex. This calls for efficient solving of the structural dynamics of any product, which is essential for quantifying its performance. Dynamic fragmentation allows efficient analysis of complex structures, as the dynamic behaviour of smaller and simpler structural fragments (substructures) are generally easier to determine. The possibilities of sharing and combining substructures from different design groups, combining experimentally and numerically obtained dynamics and the optimisation of a single subcomponent without the need for a full analysis, adds to the efficiency. Most methods which utilise this dynamic fragmentation, use the frequency domain for the re-assembly of the substructures into the full system model [5].

The frequency domain based substructuring method is however badly suited for representing the response to impact like excitations, i.e. blast, shock and impulsive loading, and the large frequency band makes this strategy also expensive. Obtaining usable measured frequency response functions, associated with those excitations, is a delicate process. The response is only obtained through several processing steps, i.e. windowing, anti-aliasing and Fourier transforms, which will unavoidably alter the information contained in the measurement. Nevertheless, the evaluation of the performance of a product subjected to this loading is essential, take for example the landing gear of an aircraft, handheld electronic devices that are dropped or a gun when firing. This led to the formulation of a transient dynamic substructuring counterpart [7, 11]. It uses impulse response functions, which are better suited for simulating these broadband loads.

In the design stages of these products, its performance to impact is analysed by assembling the impulse response functions of the substructures from an existing database or newly computed or measured data. The impulse based substructuring scheme is advantages over its frequency domain counterpart, in the ability to couple the dynamics of linear models and measurements to non-linear models [13]. This design methodology will improve the quality and design cycle time of every new product.

1.2 Research goal

The above presented design methodology, made possible by the impulse based substructuring scheme, is very attractive. The quality of the full system response will depend on the quality of the individual impulse response functions representing the *true* dynamics of the subcomponents. An accurate way of determining the linear dynamics of a component is by means of experimental testing.

To date, it is not possible to use measured impulse response functions in the impulse based substructuring scheme for finding stable and coupled full system responses. This exploratory research thesis pursues the objective of

Improvements on the impulse response computation and determining the sensitivity of measurement induced errors on the impulse based substructuring scheme.

Impact testing is widely used, but the non perfect impulse demands a deconvolution operation between the output response and the input force. Traditionally the impulse response is obtained through the frequency domain and consequently suffers from frequency domain induced errors as presented in section 1.1. The idea for a more natural time-domain deconvolved impulse response was presented in [10], but the computational cost of inverting large matrices inherent to impact testing leaves room for improvements. An inverse finite impulse response (FIR) force filter is introduced, which operates independent of the output response. The quality of the time-domain deconvolved impulse response functions, as well as the measurement induced errors are tested on the impulse based substructuring scheme. The procedures are illustrated by application to an one-dimensional bar.

1.2.1 System description

The dynamic substructuring analysis using time-domain deconvolved impulse response functions is tested on the one-dimensional polyoxymethylene (POM) bar [10], which is assumed to behave linearly. This one dimensional academical example was chosen for the easy of numerical modelling, coupling and result interpretation. The full reference system is a bar with length $2L$, as sketched in figure 1.1. The bar with free floating boundary conditions is excited with force f at its left end face. This bar is now divided into two subsystems of equal length. The impulse response functions and the introduction of a force at the interface degrees of freedom makes it possible to assemble the subsystems into the full model.

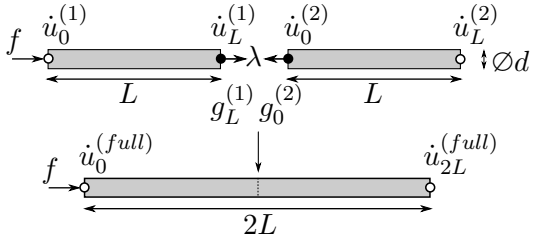

(a) *The bar and the division in subsystems*

d [mm]	L [mm]	ρ [kg/m^3]	E [GPa]
40	475.75	1420	3.75

(b) *Dimensions and material properties*

Figure 1.1: *Schematic view of the POM bar with all the necessary parameters for the dynamic substructuring process. The black dots indicate the interface degrees of freedom.*

1.3 Thesis outline

In this thesis, a time-domain deconvolution operation is presented for finding the impulse response out of multiple measurements. A selection criteria between multiple measurements and a filtering operation are also included in this time-domain approach. The quality of the measured impulse response is defined by comparing it to numerical models. These differences are used in a sensitivity analysis of the measurement induced errors on the dynamic substructuring scheme.

In figure 1.2, the workflow of the thesis is schematically shown and the chapters associated with each topic are indicated. Chapter 2 introduces the reader to the impulse response. The impulse response is obtained either by solving the equations of motions or by experimental testing

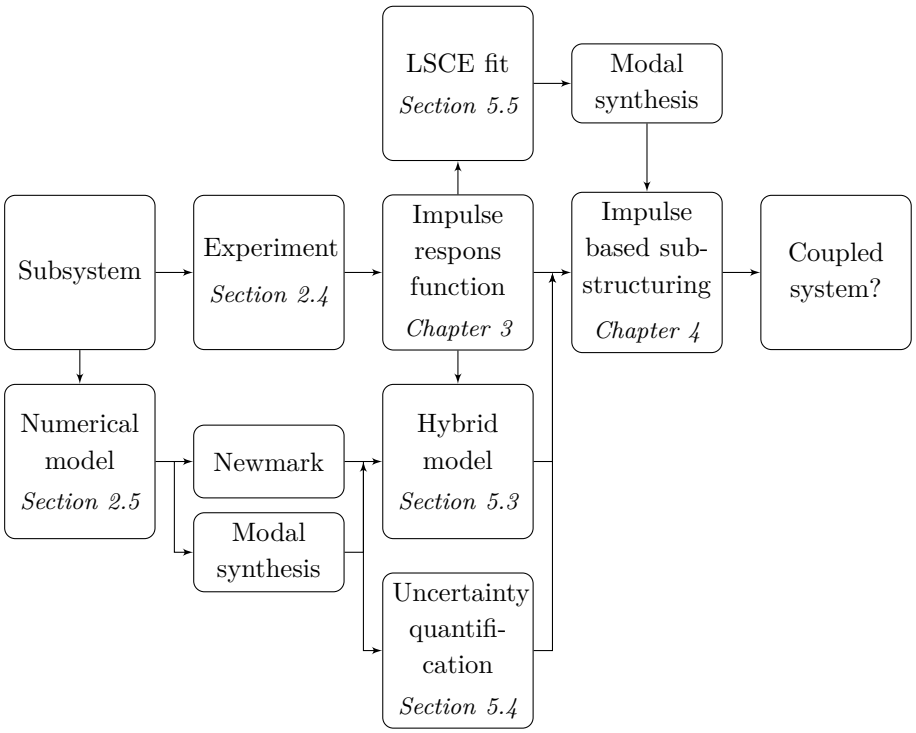

Figure 1.2: *Schematic representation of thesis content in a flowchart.*

and performing the deconvolution operation. In chapter 3, a direct time-domain deconvolution operation is presented by introduction of the inverse force filter. Operations that are conventionally associated with the frequency domain, i.e. signal filtering, the auto power spectral density and averaging, are presented in their time-domain counterparts. This chapter concludes with the method validation of the inverse force filter. Chapter 4 introduces the interface problem, which makes the coupling between substructures possible. The impulse based substructuring scheme is tested with Newmark time integrated, modal synthesised and experimental impulse response functions. In chapter 5, multiple operations are explored in the effort of coupling measured impulse response functions. Also, some of the experimental induced errors are represented by altering perfect response functions, to see their influence on the dynamic substructuring scheme.

Chapter 2

Impulse response

2.1 Introduction

The transient dynamics of a linear system is described by a signal called the *impulse response*. As the name implies, impulse response functions describe the response of a system to a unit impulse force over time. This response relates the input to the output response of a system. Convolution is a mathematical way of combining two signals to form a third signal. This chapter will state the importance of convolution because it relates the three signals of interest: the input signal, the output signal and the impulse response. If the input to a linear system isn't equal to the unit impulse, deconvolution is required for retrieving the impulse response. The transient dynamics of a mechanical system can be obtained by solving the equations of motion or by experimental testing.

2.2 Linear time-invariant systems

Any M sample signal can be decomposed into a group of M simpler impulses. Each of the group component signals contains one point of the original system while the remainder of the values being zero. Every single impulse is passed through a linear time-invariant system and the resulting output components are superimposed. This procedure can be described by a mathematical operation called *convolution*. Figure 2.1 shows that when the input signal $f[n]$ is applied to a linear system with corresponding impulse response $h[n]$, the output results in signal $u[n]$. This is equivalent to $f[n] * h[n] = u[n]$, where the symbol $*$ denotes the convolution.

The intermediate steps in the convolution operation are better shown in figure 2.2. The input force is decomposed into scaled and shifted unit impulses. Each of these single pulses will

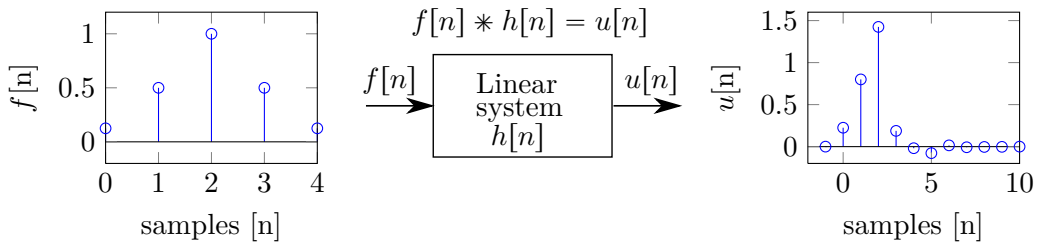

(a) *Input* **(b)** *Linear system* **(c)** *Output*

Figure 2.1: *Convolving the input with the impulse response is equal to the output.*

generate shifted and scaled impulse responses and if all these responses are superimposed, the output response is found. If the impulse response of the system is known, the output can be calculated for any input signal.

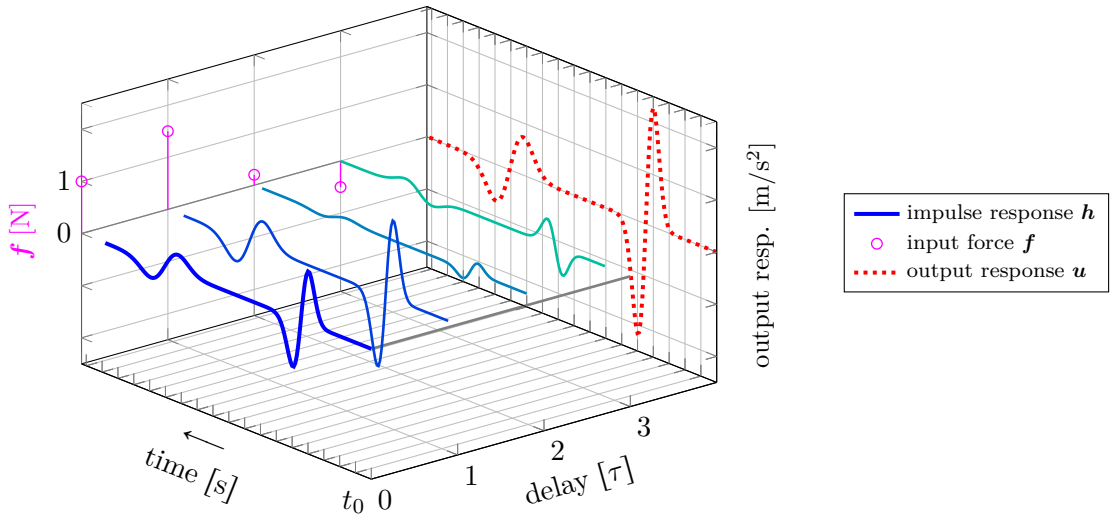

Figure 2.2: *Example of the convolution operation. The force signal* $\boldsymbol{f}$ *is decomposed into a set of scaled and shifted unit impulses:* $f(\tau)\delta(t-\tau)$*. The first decomposed impulse is indeed the unit impulse* $\boldsymbol{\delta}$*, which makes the output equal to the impulse response* $\boldsymbol{h}$*. The other three impulses also result in shifted and scaled functions of the impulse response. If the four shifted and scaled impulse responses are superimposed, the output response* $\boldsymbol{u}$ *is obtained.*

2.2.1 Convolution properties

Some of the useful properties of convolution, which will be used later in this thesis, are listed below.

- The most simple input is the unit impulse and is symbolized by $\delta[n]$. The unit impulse function shown in figure 2.3a is a Dirac delta impulse with the following properties:

$$\delta[n] \begin{cases} 1 & \text{if } n = 0 \\ 0 & \text{otherwise} \end{cases} \tag{2.1}$$

  and will give direct access to the impulse response if it is the input to the system, according to figure 2.3. This property makes the unit delta function the identity for convolution.

- The commutative property for convolution states that the input and impulse response can be changed, without changing the output.

$$f[n] * h[n] = h[n] * f[n] = u[n] \tag{2.2}$$

  This will turn out to be a useful mathematical property but does not have any physical meaning.

- As shown in figure 2.1, an input signal $f[n]$ enters a linear system with an impulse response $h[n]$, resulting in an output signal $u[n]$. If M and Q are respectively the sample lengths of $f[n]$ and $h[n]$, than the output signal $u[n]$, resulting from this convolution operation, consists of $N = M + Q - 1$ samples.

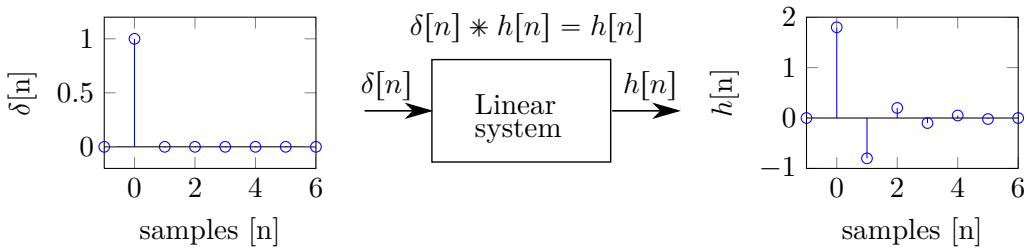

(a) *Unit impulse* **(b)** *Linear system* **(c)** *Impulse response*

Figure 2.3: *Unit delta function as the input for a linear system and the output is the impulse response.*

2.3 Time response of dynamical systems

All the dynamics of a mechanical system are stored in the impulse response. If the point of observation is changed to the frequency domain, the same dynamics are stored in the frequency response. Lets start with the equations of motion and derive the frequency and impulse response from here.

$$\boldsymbol{M}\ddot{\boldsymbol{u}}(t) + \boldsymbol{C}\dot{\boldsymbol{u}}(t) + \boldsymbol{K}\boldsymbol{u}(t) = \boldsymbol{f}(t) \tag{2.3}$$

where the $\boldsymbol{M}$, $\boldsymbol{C}$, and $\boldsymbol{K}$ are respectively the mass, damping and stiffness matrices, $\boldsymbol{u}(t)$ the set of degrees of freedom and $\boldsymbol{f}(t)$ the external applied forces. Equation (2.3) can be converted to the frequency domain by using a Fourier transform, where $\ddot{\boldsymbol{u}}(\omega) = j\omega\dot{\boldsymbol{u}}(\omega) = -\omega^2\boldsymbol{u}(\omega)$. The equations of motion now write:

$$(-\omega^2\boldsymbol{M} + j\omega\boldsymbol{C} + K)\boldsymbol{u}(\omega) = \boldsymbol{Z}(\omega)\boldsymbol{u}(\omega) = \boldsymbol{f}(\omega) \tag{2.4}$$

The dynamic stiffness is replaced by the matrix $\boldsymbol{Z}(\omega)$. The response of the degrees of freedom to an external applied force can be found by rearranging equation (2.4).

$$\boldsymbol{u}(\omega) = \boldsymbol{Z}^{-1}(\omega)\boldsymbol{f}(\omega) = \boldsymbol{Y}(\omega)\boldsymbol{f}(\omega) \tag{2.5}$$

The flexibility matrix $\boldsymbol{Y}(\omega)$ is the inverse of the dynamic stiffness and contains the frequency response functions of all discretised degrees of freedom. The transient response of a system, excited by an external force, is obtained by the inverse Fourier transform:

$$\boldsymbol{u}(t) = \boldsymbol{H}(t) * \boldsymbol{f}(t) = \int_{\tau=-\infty}^{\infty} \boldsymbol{H}(t-\tau)\boldsymbol{f}(\tau)d\tau \tag{2.6}$$

where $\boldsymbol{H}$(t) is the impulse response, describing the dynamics of the system. So the impulse response $\boldsymbol{H}(t)$ is equal to the frequency response $\boldsymbol{Y}(\omega)$ when the domain of observation is shifted from time to frequency. It can also be seen that convolution in the time domain is equal to multiplication in the frequency domain.

The integral of equation (2.6) is known as the Duhamel integral. If the system is assumed to be at rest before $t = 0$, the interval of the definite integral runs from $\tau = 0$ to $\tau = t$. The transient response can similarly be defined for the velocities and accelerations. By substituting the mobility $\dot{\boldsymbol{H}}$ and the accelerance $\ddot{\boldsymbol{H}}$ in equation (2.6), the following expressions are found:

$$\dot{\boldsymbol{u}}(t) = \int_{\tau=0}^{t} \dot{\boldsymbol{H}}(t-\tau)\boldsymbol{f}(\tau)d\tau \tag{2.7}$$

$$\ddot{\boldsymbol{u}}(t) = \int_{\tau=0}^{t} \ddot{\boldsymbol{H}}(t-\tau)\boldsymbol{f}(\tau)d\tau \tag{2.8}$$

The output response at time t can be interpret as an infinite sum of the impulse responses to the infinitesimal impulses $\boldsymbol{f}(\tau)d\tau$ before time t. In this notation, each impulse at time τ gives a contribution through the flipped impulse response, so from t to τ.

2.4 Experimental dynamics and deconvolution

The goal of experimental dynamics is to determine the dynamics of a physical system by measuring discrete input and output signals on discretised points on the structure. Sensors are used to determine the amplitude of the input force and output motion as a function of time. The excitation force to the system can either be applied using a shaker or impact hammer. An example of the force $\boldsymbol{f}(t)$ exerted by an impact hammer is shown in figure 3.8a. The impact is assumed to only take place between the left and right bound of the rectangle window. Although this impact has only a duration of 0.9 ms, it is nowhere near equal to the perfect unit impulse, as introduced in section 2.2. Due to this non perfect impulse the output of the linear system will not give access to the impulse response $\boldsymbol{h}(t)$, but the output response $\boldsymbol{u}(t)$. The output acceleration due the impact as a function of time is measured with an accelerometer and shown in figure 3.8c. An output window is used to ensure that the boundaries of the signal are equal to zero, this is done to reduce the (frequency domain) effect of *leakage*.

A deconvolution operation is necessary to compensate for the non perfect impact. Traditionally, this deconvolution operation is performed in the frequency domain. This means that the input and output signals needs to be converted to the frequency domain, by means of the discrete Fourier transform.

The discrete Fourier transform is used to decompose the original time-domain signal as a sum of waves, mathematically represented by sine and cosine functions to describe the frequency spectrum. For the derivation of the discrete Fourier transform, lets start with the continuous Fourier transform

$$y(f) = \mathcal{F}[y(t)](f) \tag{2.9}$$

$$= \int_{t=-\infty}^{\infty} y(t)e^{-2i\pi ft}\,dt \tag{2.10}$$

If the switch is now made to discrete signals, $y(t) \rightarrow y[t_k]$, where $t_k = k\Delta$ with $k = 0, \ldots, N-1$, the discrete Fourier transform writes

$$y[f] = \sum_{k=0}^{N-1} y[t_k]e^{-2\pi ifk/N} \tag{2.11}$$

Note that due to *aliasing*, the frequency domain data is limited to the Nyquist frequency: $k = N/2$. This happens because the periods of the input data become split into positive and negative frequency complex components of the single sine wave.

The time-domain force and acceleration signals are transformed to the frequency domain and respectively shown in figures 3.8b and 3.8d. A simple division of $\boldsymbol{U}(\omega)/\boldsymbol{F}(\omega)$ results in the frequency response function $\boldsymbol{H}(\omega)$, as shown in figure 3.8f. Note that this is only true for a single measurement. For multiple measurements, the frequency response is estimated according to equation (3.28). Finally, the inverse discrete Fourier transform computes the desired impulse response function, which is shown in figure 3.8e.

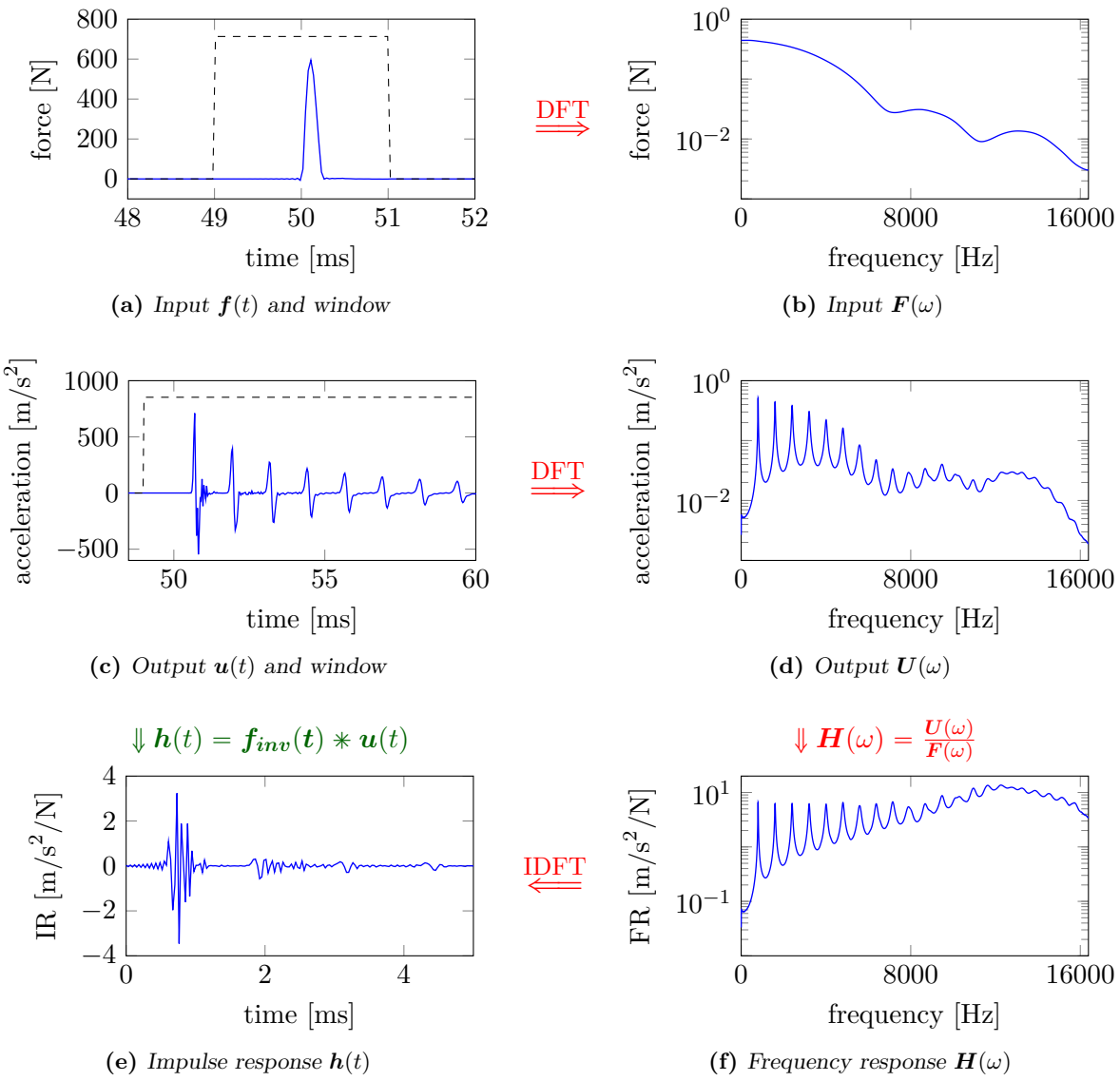

(a) *Input* $\boldsymbol{f}(t)$ *and window* **(b)** *Input* $\boldsymbol{F}(\omega)$

(c) *Output* $\boldsymbol{u}(t)$ *and window* **(d)** *Output* $\boldsymbol{U}(\omega)$

(e) *Impulse response* $\boldsymbol{h}(t)$ **(f)** *Frequency response* $\boldsymbol{H}(\omega)$

Figure 2.4: *Flowchart showing two paths (red and green) from the input and output response to the impulse response. Left the time and right the frequency domain.*

2.4.1 Measurement of POM bar

The force input and the velocity output are measured on the locations given in figure 1.1a. First, the homogeneous full bar was measured before the subsystems were cut to length, such that the reference configuration had no additional joint stiffness and damping. The gathered experimental data will be used in chapter 3 to test the proposed deconvolution operation and in chapter 4 to couple the substructures into the full system.

The bar is supported by a lightly inflated bike inner tube to represent the free floating boundary conditions, as shown in figure 2.5a. The suspension of the bar is not ideal since it introduces some systematic error into the measurement, i.g. the system is more damped, the rigid body mode is no longer at zero hertz and the induced moment around the inner tube introduces bending modes.

An impact hammer[1] was used to excite the system in the longitudinal (axial) direction. The impact hammer with aluminium tip hit the bar on an aluminium nut, which was glued to the structure, see figure 2.5b. The combination of the two materials with high stiffness ensured a very short impact time, i.e. distribution of the energy at a large bandwidth. During the dynamic identification of the system, a roving hammer approach was used. This means that the output is fixed and the impulse response functions are measured for multiple inputs, this corresponds to measuring elements from a single row of the impulse response matrix. Recommended would however be to use a single input multiple output system. This will reduce the deconvolution cost, it will get rid of the linearisation error made by the amplitude of the replicate excitation forces and it will reduce the error of not exciting the system at the same place and in the correct direction.

A laser vibrometer[2] as well as an acceleration sensor[3] were used to measure the output responses at the end faces. The displacement response was of very low quality and the acceleration response was abandoned due to reasons given in chapter 4. Recommended for future measurements would be to only use the laser vibrometer for the velocity response. This would also minimise the added sensor mass.

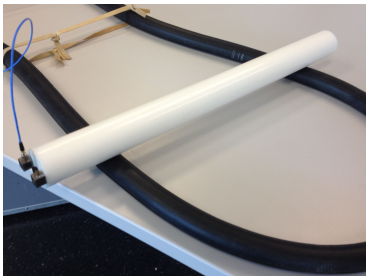

(a) *Suspension of the bar*

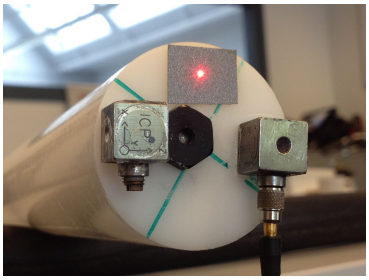

(b) *End face at length* $0L$

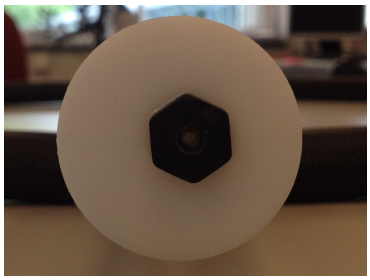

(c) *End face at length* L *and* $2L$

Figure 2.5: *Measurement setup.*

Dynamics of the subsystem

The spectral dynamics of the two boundary degrees of freedom of the subsystem are shown in figure 2.6, for the average of five replicate measurements. The signals have a sampling rate of 32.8 kHz and a blocksize of 16384 samples. The frequency response functions shows the fundamental frequency at 1.6 kHz. This frequency can be determined by the speed of the wave through the material and the wave length (for the subsystem equal to two times length L). The additional peaks in the frequency response should theoretically be the integer multiple of the fundamental frequency. A simple doubly clamped beam, such as a guitar snare, will show a similar response [14]. The additional smaller peaks in the signal can be bending modes due to the suspension and direction of impact, or the additional sensor mass and stiffness. The coherence function is used as a data quality assessment tool which identifies how much of the output signal is related to the measured input signal. It shows that this signal starts to deteriorate as well as the frequency response function above 6.5 kHz. The impulse response functions are shown in figures 2.7 and 2.9. The response shows a travelling wave, which is a superposition of multiple standing waves. Again, the wave speed and the length of the bar determine the period time.

[1] PCB Piezotronics: 086C03, serial number 24524.

[2] Polytec Scanning Vibrometer OFV-505, displacement and velocity sensitivity of respectively 5.12 µm/V and 125 mm/(s V).

[3] PCB Piezoelectronics: Y356A32, serial number 32652

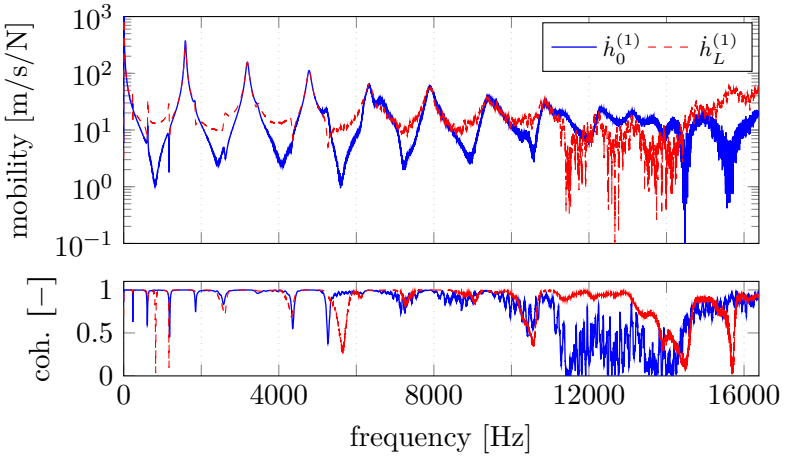

Figure 2.6: *Frequency response function and corresponding coherence of the subsystems.*

2.5 Impulse response simulation

To solve the structural dynamic equations of motion under arbitrary excitation, two approaches can be considered, namely modal superposition techniques and direct time- integration methods. Both methods will be presented in this section and used to find the impulse response functions of the bar test case. The equations of motion are defined using eleven bar elements per unit of length L with Reyleigh damping and material properties as shown in figure 1.1. The simulated response is compared to the measured response and used throughout this thesis.

2.5.1 Newmark time integration

The direct time integration scheme computes the conditions at the proceeding time step from the equations of motion, given in equation (2.3). Necessary are the initial conditions, i.e. velocity and displacement $(\dot{\boldsymbol{u}}_0, \boldsymbol{u}_0)$ and the finite difference equations:

$$\ddot{\boldsymbol{u}}_n = \lim_{\Delta t \to 0} \frac{\dot{\boldsymbol{u}} - \dot{\boldsymbol{u}}(t_n \mp \Delta t)}{\pm \Delta t} \qquad \dot{\boldsymbol{u}}_n = \lim_{\Delta t \to 0} \frac{\boldsymbol{u} - \boldsymbol{u}(t_n \mp \Delta t)}{\pm \Delta t} \tag{2.12}$$

An efficient single-step integration method was introduced by Newmark [9], which is commonly used in the field of structural dynamics for large degrees of freedom systems. The state vector at the next time step t_{n+1} is deduced from information at the current time step using a Taylor series expansion

$$f(t_n + \Delta t) = f(t_n) + \Delta t \dot{f}(t_n) + \frac{\Delta t^2}{2!} \ddot{f}(t_n) + \frac{\Delta t^3}{3!} \dddot{f}(t_n) + R_s \tag{2.13}$$

where R_s are the higher order terms. If the higher order terms are neglected, the displacement and velocity at the next time step can be approximated as follows:

$$\dot{\boldsymbol{u}}_{n+1} = \dot{\boldsymbol{u}}_n + \Delta t \ddot{\boldsymbol{u}}_n + \gamma \Delta t^2 \dddot{\boldsymbol{u}}_n \tag{2.14}$$

$$\boldsymbol{u}_{n+1} = \boldsymbol{u}_n + \Delta t \dot{\boldsymbol{u}}_n + \frac{\Delta t^2}{2} \ddot{\boldsymbol{u}}_n + \beta \Delta t^3 \dddot{\boldsymbol{u}}_n \tag{2.15}$$

The integration constants β and γ are introduced. The finite difference principles also allows for the calculation of the jerk, by assuming constant acceleration between the time steps. If this

is applied to equations (2.14) and (2.15), the approximations formulas for the Newmark scheme become:

$$\dot{\boldsymbol{u}}_{n+1} = \dot{\boldsymbol{u}}_n + (1-\gamma)\Delta t\ddot{\boldsymbol{u}}_n + \gamma\Delta t\ddot{\boldsymbol{u}}_{n+1} \tag{2.16}$$

$$\boldsymbol{u}_{n+1} = \boldsymbol{u}_n + \Delta t\dot{\boldsymbol{u}}_n + (\tfrac{1}{2}-\beta)\Delta t^2\ddot{\boldsymbol{u}}_n + \beta\Delta t^2\ddot{\boldsymbol{u}}_{n+1} \tag{2.17}$$

The proceeding acceleration step $\ddot{\boldsymbol{u}}_{n+1}$ can be solved if equations (2.16) and (2.17) are substituted in the linear set of equations of motion, equation (2.3):

$$\boldsymbol{S}\ddot{\boldsymbol{u}}_{n+1} = \boldsymbol{f}_{n+1} - \boldsymbol{C}\left(\dot{\boldsymbol{u}}_n + (1-\gamma)\Delta t\ddot{\boldsymbol{u}}_n\right) - \boldsymbol{K}\left(\boldsymbol{u}_n + \Delta t\dot{\boldsymbol{u}}_n + (\tfrac{1}{2}-\beta)\Delta t^2\ddot{\boldsymbol{u}}_n\right) \tag{2.18}$$

where the constant effective stiffness matrix $\boldsymbol{S}$ is defined as:

$$\boldsymbol{S} = \boldsymbol{M} + \gamma\Delta t\boldsymbol{C} + \beta\Delta t^2\boldsymbol{K} \tag{2.19}$$

The inverse of the effective stiffness matrix thus only needs to be calculated one. The impulse response function of a system can be found if stimulated with an unit impulse. The initial *velocity step* is found by solving the momentum equation

$$\boldsymbol{M}(\dot{\boldsymbol{u}}_{0^+} - \dot{\boldsymbol{u}}_{0^-}) = \int_{t=0^-}^{0^+} \boldsymbol{f}(t)dt \tag{2.20}$$

The system is at rest before the unit impulse at degree of freedom $_j$ is applied, so the initial velocity writes $\dot{\boldsymbol{u}}_0 = \boldsymbol{M}^{-1}\mathbf{1}_j$ and the initial displacement $\boldsymbol{u}_0 = \mathbf{0}$. As always, the initial velocity is solved through the equations of motion. Note that the initial applied force can also be used in formulating the initial conditions for the velocity and displacements [12]. If compared to the impulse response found by modal superposition, in section 2.5.2, the initial applied force introduces a delay of Δt and lacks information about the initial velocity. In order to keep the models consistent, the initial applied force is not used.

Numerical solutions of POM bar

The Newmark time integration algorithm is used to compute the transient response of the system. The implicit average constant acceleration scheme $\gamma = \frac{1}{2}$ and $\beta = \frac{1}{4}$ is unconditionally stable, but the high frequency impact response nevertheless requires a very small time step. The step is chosen equal to the Courant's condition, which states that the time step must be smaller than the time for an elastic wave to transverse an element. The model of the bar consists of eleven elements with Reyleigh damping, this corresponds to a time step of 1/65.5 kHz, twice the sampling rate of the measurement. The result is shown in figure 2.7, where the Newmark time intergated response if plotted next to that of the measurement.

2.5.2 Modal synthesis

Impulse response functions can also be obtained from modal synthesis. It uses modal parameters to build up the response [4]. Numerical and empirical data can both give access to these modal parameters. An inverse Fourier transform of the frequency response function gives the following

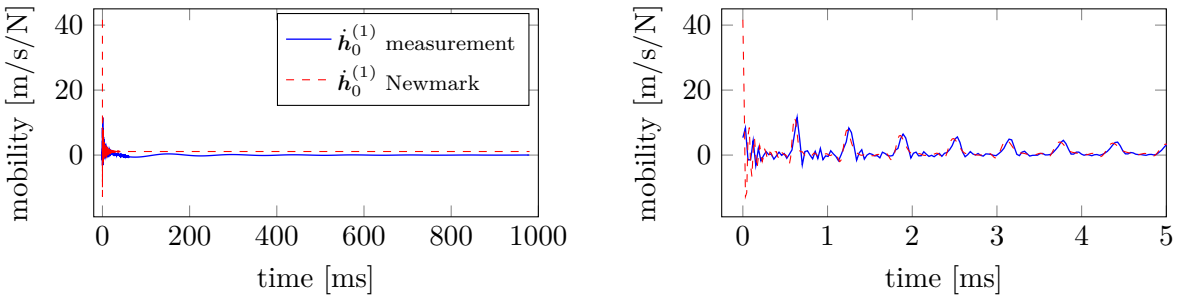

(a) *Impulse response of* $\dot{h}_0^{(1)}$ **(b)** *First periods of* $\dot{h}_0^{(1)}$

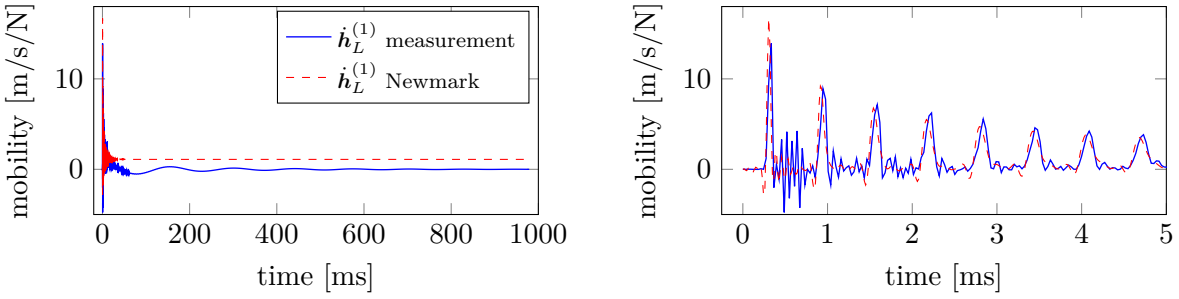

(c) *Impulse response of* $\dot{h}_L^{(1)}$ **(d)** *First periods of* $\dot{h}_L^{(1)}$

Figure 2.7: *Transient comparison of the measurement and the Newmark time integration.*

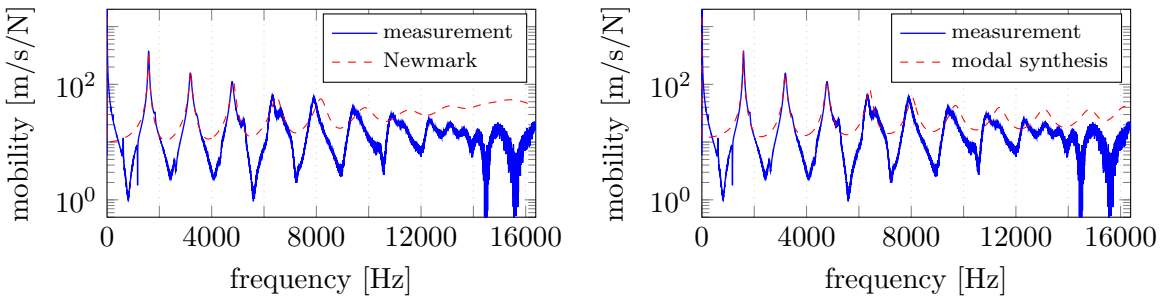

(a) *Measurement and Newmark simulation* **(b)** *Measurement and modal synthesis*

Figure 2.8: *Spectral comparison of measurement and numerical models.*

expression:

$$\boldsymbol{h}(t) = \text{IFFT}\left(\boldsymbol{H}(\omega)\right) \tag{2.21}$$

$$= \text{IFFT}\left(\sum_{j=1}^{n}\left(\frac{\boldsymbol{R}_{(j)}}{i\omega - \lambda_{(j)}} + \frac{\overline{\boldsymbol{R}}_{(j)}}{i\omega - \overline{\lambda}_{(j)}}\right)\right) \tag{2.22}$$

$$= \sum_{j=1}^{n}\left(\boldsymbol{R}_{(j)}e^{\lambda_{(j)}t} + \overline{\boldsymbol{R}}_{(j)}e^{\overline{\lambda}_{(j)}t}\right) \tag{2.23}$$

$$= 2Re\left(\sum_{j=1}^{n}\boldsymbol{R}_{(j)}e^{\lambda_{(j)}t}\right) \tag{2.24}$$

A bar denotes the complex conjugate. The system pole $\lambda_{(j)}$ contains the frequency and damping components for mode $_{(j)}$ and the residual is defined as $\boldsymbol{R}_{(j)} = \frac{\boldsymbol{x}_{(j)}\boldsymbol{x}_{(j)}^T}{\mu_{(j)}}$. If a system has a large number of degrees of freedom, the sum may be truncated to a subset of $k \leqslant n$ modes to find the approximate solution. Equation (2.24) can be written in an alternative form to better show the superposition of sinusoidal functions:

$$\boldsymbol{h}(t) = \sum_{j=1}^{n} \frac{\boldsymbol{x}_{(j)}\boldsymbol{x}_{(j)}^T}{\mu_{(j)}} \frac{1}{\omega_{d_{(j)}}} \int_0^t e^{-\zeta\omega_{(j)}(t-\tau)} \sin(\omega_{d_{(j)}}(t-\tau))\boldsymbol{\delta}(\tau)\, d\tau \tag{2.25}$$

This equation will give access to the transmissibility since the external load is a delta impulse. The damping is the cause for the exponential decaying function and the delay in the sine function. The derivative of the temporal term of equation (2.25) will give the mobility function and the impulse response will be a superposition of delayed cosine functions. In the same manner, the double derivative will give the acceleration and is a superposition of delayed negative sine functions.

Analytical solutions of POM bar

The system response is expressed as a superposition of its eigenmodes. The impulse response of the modal synthesis can be seen as a discretised signal of the underlying continuum model, similar to that of the experimentally obtained response. The solution, in contrast to the time integration, is therefore independent of the sampling frequency and is set equal to the experimental time step for the ease of comparison, see figure 2.9.

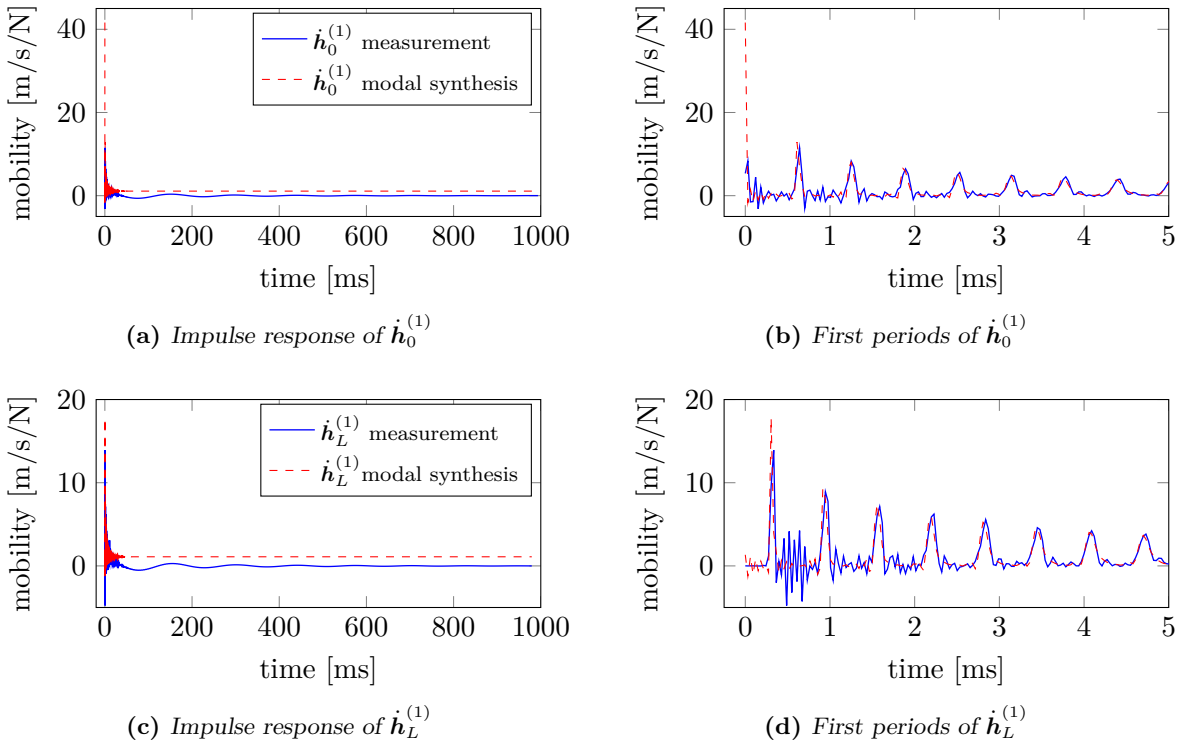

(a) *Impulse response of* $\dot{\boldsymbol{h}}_0^{(1)}$

(b) *First periods of* $\dot{\boldsymbol{h}}_0^{(1)}$

(c) *Impulse response of* $\dot{\boldsymbol{h}}_L^{(1)}$

(d) *First periods of* $\dot{\boldsymbol{h}}_L^{(1)}$

Figure 2.9: *Comparison of the experimental and modal synthesised impulse response functions.*

Chapter 3

Time-domain deconvolution

3.1 Introduction

In this chapter, the idea of a more natural time-domain method for finding the impulse response is explored. Traditionally the dynamics of the system is found in the frequency domain by a simple division. The time-domain equivalent is the deconvolution operation between the output $\boldsymbol{u}(t)$ and the input force $\boldsymbol{f}(t)$. There is no need for Fourier transforms and windowing functions, which could make the time-domain approach more accurate and or more efficient. The common theme is the following general method: the Cauchy product is written in tensor form and the impulse response is found by solving a least-squares linear system.

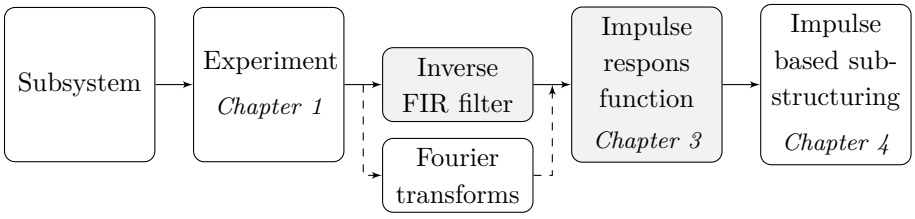

Figure 3.1: *Current chapter in relation to other chapters in this thesis.*

3.2 Linear least-square system

Finite impulse response functions can be obtained from simulations and experiments. In the field of experimental dynamics, discrete signals originating from input and output sensors are gathered. According to equation (2.6), the deconvolution of the measured input force filter and the output displacement produces the desired impulse response. This continuous convolution integral needs the be discretised in order to deal with the finite number of samples. This operator is

$$u_n = \sum_{i=1}^{n-1} h_{n-i+1} f_i \, \Delta t \tag{3.1}$$

also known as the one dimensional *Cauchy* product. The force function can be decomposed into a set of impulses, as shown in figure 3.2. The forward difference approximation will underestimate the elementary impulses in the first half of the force signal and will overestimate in the second half of the force signal. Due the nearly symmetric non perfect impacts, the total sum of the impulses will be correctly estimated. The trapezoidal approximation was not used since it would

introduce a delay in the response. The total response $\boldsymbol{u}$ at time t can be found by summing all the responses due to the elementary impulses acting at all times τ.

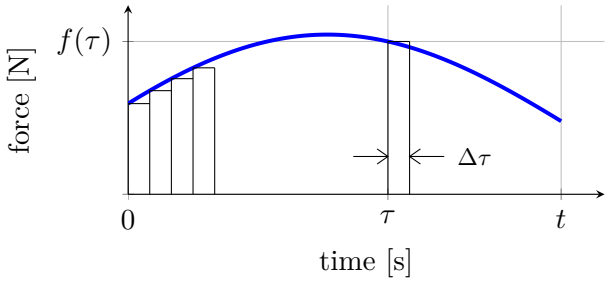

Figure 3.2: *An arbitrary forcing function as a set of elementary impulses.*

The commutative property of convolution, equation (2.2), makes it possible to flip either the impulse response or the force function:

$$u_n = \sum_{i=1}^{n-1} f_{n-i+1} h_i \, \Delta t \tag{3.2}$$

This notation is beneficial over equation (3.1), assuming that the length of the input force $\boldsymbol{f}$ is shorter than the output response $\boldsymbol{u}$, when writing the summation into a tensor multiplication. For this one dimensional convolution, the windowed excitation force $\boldsymbol{f}$ consists of M samples. The dynamics of the system is stored in array $\boldsymbol{h}$, which has a size of $Q = N + M - 1$ samples and lastly, the measured output $\boldsymbol{u}$ has N samples. Since the duration of the excitation force used for impact analysis is around 0.9 ms and the output response in the order of one thousand milliseconds, the following expressions will assume that $N \geqslant M$.

The discrete convolution operation of equation (3.2) can be constructed as a tensor multiplication, where one of the inputs is converted into a *Toeplitz* matrix [2]. Each column of the matrix stores the values of $\boldsymbol{f}$ as they slide along the tapped delay line[1]. The number of elements in the tapped delay line is equal to the number of elements in $\boldsymbol{h}$.

$$\underbrace{\begin{bmatrix} u_1 \\ u_2 \\ \vdots \\ u_N \end{bmatrix}}_{N \text{ by } 1} = \underbrace{\begin{bmatrix} f_1 & 0 & \cdots & 0 \\ \vdots & f_1 & & \vdots \\ f_M & \vdots & \ddots & 0 \\ 0 & f_M & & f_1 \\ \vdots & & \ddots & \vdots \\ 0 & \cdots & 0 & f_M \end{bmatrix}}_{N \text{ by } Q=N-M+1} \underbrace{\begin{bmatrix} h_1 \\ h_2 \\ \vdots \\ h_Q \end{bmatrix}}_{Q=N-M+1 \text{ by } 1} \Delta t \tag{3.3}$$

$$\boldsymbol{u} = \boldsymbol{F}\boldsymbol{h} \, \Delta t \tag{3.4}$$

It can be seen that $\boldsymbol{F}$ is by construction a rank-deficient matrix. One useful solutions to equation (3.4) is given by the least squares minimum norm:

$$\boldsymbol{h}_{ls} = (\boldsymbol{F}^T\boldsymbol{F})^{-1}\boldsymbol{F}^T\boldsymbol{u} \, \tfrac{1}{\Delta t} = \boldsymbol{F}^{inv}\boldsymbol{u} \, \tfrac{1}{\Delta t} \tag{3.5}$$

The accuracy of this operation depends on the number of columns in $\boldsymbol{F}$ and will be examined in section 3.6. Notice that when both sides of equation (3.5) are multiplied by $\boldsymbol{F}$, the original

[1] A more elegant way of defining the Toeplitz matrix is by using index notations: $F_{ij} = f_{i-j}$.

equation (3.4) is obtained, since:

$$(\boldsymbol{F}^T\boldsymbol{F})^{-1}\boldsymbol{F}^T\boldsymbol{F} = \boldsymbol{I} \tag{3.6}$$

The inverse filter matrix equivalent must thus be the pseudo inverse of the Toeplitz matrix

$$\boldsymbol{F}^{inv} = (\boldsymbol{F}^T\boldsymbol{F})^{-1}\boldsymbol{F}^T = \boldsymbol{R}^{-1}\boldsymbol{F}^T \tag{3.7}$$

The inverse FIR filter matrix of equation (3.7) is sufficient in solving the deconvolution operation, however the drawback is that the dimensions are prescribed by the output response length N. Take for example the measurement conducted in this thesis: $N = 32\,768$ and $M = 63$. Finding the inverse of a very large matrix is costly and therefore this tensor multiplication is not applicable for the field of experimental dynamics.

3.3 Inverse force filter

Instead of a tensor multiplication, as presented in the previous section, a first order tensor is explored that if convolved with the force filter, results in the unit impulse. This first order tensor is the inverse of the force filter and will be called the inverse force filter $\boldsymbol{f}^{inv}$. It has to satisfy the equation that holds for all inverses:

$$\boldsymbol{f} * \boldsymbol{f}^{inv} = \boldsymbol{\delta} \tag{3.8}$$

Because of the similarity with equation (3.6), the inverse filter $\boldsymbol{F}^{inv}$ is the matrix counterpart of the inverse force filter vector $\boldsymbol{f}^{inv}$. The deconvolution operation can be performed by convolving the output $\boldsymbol{u}$ with the inverse filter $\boldsymbol{f}^{inv}$

$$\hat{\boldsymbol{h}} = \boldsymbol{\delta} * \boldsymbol{h} = \boldsymbol{f} * \boldsymbol{f}^{inv} * \boldsymbol{h} = \boldsymbol{f}^{inv} * \boldsymbol{u}\,\frac{1}{\Delta t} \tag{3.9}$$

The approximated impulse response $\hat{\boldsymbol{h}}$ is the true impulse response if $\boldsymbol{f}^{inv}$ is indeed the inverse filter to $\boldsymbol{f}$, i.e. if equation (3.8) is satisfied. Formally, the inverse filter of a finite impulse response must be an infinite impulse response. Still it is possible to approximate a finite inverse force filter that is shorter than N, resulting in a efficient impulse response estimation. Since the deconvolution is performed using a convolution operation, the inverse filter length is no longer dependent on the length of the output response.

Now let us define the properties of the encountered matrices. If $\boldsymbol{F}$ is multiplied with any array, valid convolution is obtained. If $\boldsymbol{F}^T$ is multiplied with any array, the linear correlation is found. This is due to the fact that the transpose of the matrix eliminates the flip of the filter, which distinguishes the convolution from the correlation operation. So $\boldsymbol{F}^T\boldsymbol{F} = \boldsymbol{R}$ is equivalent to the linear auto-correlation of $\boldsymbol{r} = \boldsymbol{f} \star \boldsymbol{f}$. The correlation matrix $\boldsymbol{R}$ is examined for a filter f_n with $n = 1, 2, 3$ and Q equal to five.

$$\boldsymbol{R} = \boldsymbol{F}^T\boldsymbol{F} \tag{3.10}$$

$$= \begin{bmatrix} f_1 & f_2 & f_3 & 0 & 0 & 0 & 0 \\ 0 & f_1 & f_2 & f_3 & 0 & 0 & 0 \\ 0 & 0 & f_1 & f_2 & f_3 & 0 & 0 \\ 0 & 0 & 0 & f_1 & f_2 & f_3 & 0 \\ 0 & 0 & 0 & 0 & f_1 & f_2 & f_3 \end{bmatrix} \begin{bmatrix} f_1 & 0 & 0 & 0 & 0 \\ f_2 & f_1 & 0 & 0 & 0 \\ f_3 & f_2 & f_1 & 0 & 0 \\ 0 & f_3 & f_2 & f_1 & 0 \\ 0 & 0 & f_3 & f_2 & f_1 \\ 0 & 0 & 0 & f_3 & f_2 \\ 0 & 0 & 0 & 0 & f_3 \end{bmatrix} \tag{3.11}$$

$$= \begin{bmatrix} f_1^2+f_2^2+f_3^2 & f_1f_2+f_2f_3 & f_1f_3 & 0 & 0 \\ f_1f_2+f_2f_3 & f_1^2+f_2^2+f_3^2 & f_1f_2+f_2f_3 & f_1f_3 & 0 \\ f_1f_3 & f_1f_2+f_2f_3 & f_1^2+f_2^2+f_3^2 & f_1f_2+f_2f_3 & f_1f_3 \\ 0 & f_1f_3 & f_1f_2+f_2f_3 & f_1^2+f_2^2+f_3^2 & f_1f_2+f_2f_3 \\ 0 & 0 & f_1f_3 & f_1f_2+f_2f_3 & f_1^2+f_2^2+f_3^2 \end{bmatrix} \tag{3.12}$$

$$= \begin{bmatrix} r_0 & r_{-1} & r_{-2} & 0 & 0 \\ r_1 & r_0 & r_{-1} & r_{-2} & 0 \\ r_2 & r_1 & r_0 & r_{-1} & r_{-2} \\ 0 & r_2 & r_1 & r_0 & r_{-1} \\ 0 & 0 & r_2 & r_1 & r_0 \end{bmatrix} \tag{3.13}$$

It is observed that the full auto-correlation vector $\boldsymbol{r}$ is positioned in both the middle row and column, see equation (3.13). This auto-correlation vector of an arbitrary filter will result in a symmetric signal. It is also seen that the correlation matrix $\boldsymbol{R}$ is symmetric and full rank and it's inverse $\boldsymbol{R}^{-1}$ will therefore also be symmetric and full rank. Given the 35 components of $\boldsymbol{F}$, it is easy to compute the 15 components of $\boldsymbol{R}$, but given $\boldsymbol{R}$ it is impossible to compute the components of $\boldsymbol{F}$.

Equation (3.8) will be essential in finding the inverse FIR filter. If the force in this convolution operation is tranformed into a Toeplitz matrix, similar to that of equation (3.3), the following form is found:

$$\boldsymbol{F}\boldsymbol{f}^{inv} = \boldsymbol{\delta} \tag{3.14}$$

$$\boldsymbol{F}^T\boldsymbol{F}\boldsymbol{f}^{inv} = \boldsymbol{F}^T\boldsymbol{\delta} \tag{3.15}$$

$$\boldsymbol{R}\boldsymbol{f}^{inv} = \boldsymbol{F}^T\boldsymbol{\delta} \tag{3.16}$$

$$\boldsymbol{f}^{inv} = \boldsymbol{R}^{-1}\boldsymbol{F}^T\boldsymbol{\delta} \tag{3.17}$$

$$\tag{3.18}$$

The expression $\boldsymbol{F}^T\boldsymbol{\delta}$ is equal to the reversed force vector, padded with $Q-M$ zeros. The inverse FIR filter $\boldsymbol{f}^{inv}$ is used in equation (3.9) to solve for the impulse response of a linear system.

3.3.1 Inverse FIR filter of non-perfect impact

A non-perfect impulse response created with an impact hammer is show in figure 3.3a. This bell shaped function clearly does not represents a unit impulse. The output response needs to be convolved with the inverse force filter to find the impulse response, as equation (3.9) prescribes. The inverse force filter to the non-perfect impact is shown in figure 3.3b and consist of Q samples.

In order to check the accuracy of the inverse force filter, the force function is convolved with the inverse force filter. The output should result in the unit impulse, as shown in figure 3.3c. The theoretical value of the sum of all the values is one and will be used as the benchmark for the accuracy of the inverse filter. The accuracy of the inverse force filter is determined by the number of columns Q in the Toeplitz matrix $\boldsymbol{F}$ and the conditioning of the correlation matrix $\boldsymbol{R}$, which will be studied in section 3.6.

3.3.2 Impulse response reconstruction

The impulse response function is found by convolution of the output $\boldsymbol{u}$ with the inverse FIR filter $\boldsymbol{f}^{inv}$, as shown in equation (3.9). The resulting sample length of $\hat{\boldsymbol{h}}$ is due to the convolution equal to $N+Q-1$. This is longer than the properties of convolution in section 2.2.1 define

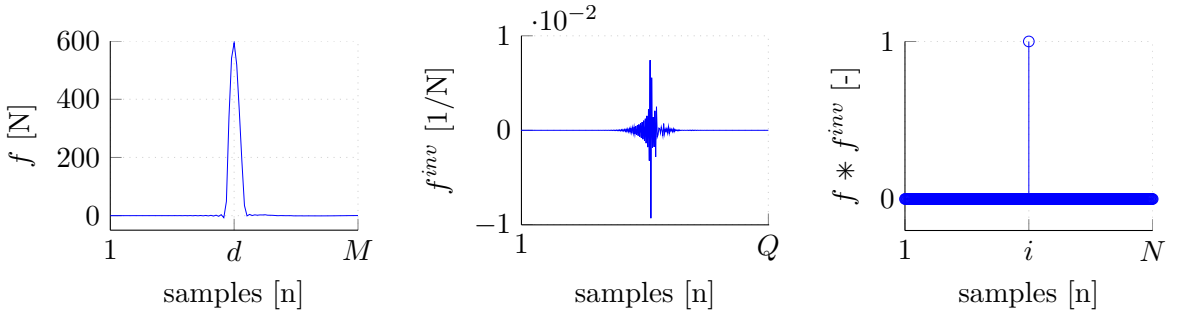

(a) *Non-perfect impact* **(b)** *Inverse force filter* **(c)** *Unit impulse with delay*

Figure 3.3: *The inverse FIR filter originated from a non-perfect impulse and the accuracy check.*

for the length of the impulse response. The sample length of the impulse response $\boldsymbol{h}$ should be equal to $Q = N - M + 1$.

The impulse response is indeed present in the signal and only needs to be filtered out. The reconstruction of the unit impulse $\boldsymbol{f}^{inv} * \boldsymbol{f} = \boldsymbol{\delta}$ is used in this process. The delay i at which the unit impulse is equal to one, as shown on the x-axis in figure 3.3c, is used to define the start point of the impulse response in $\hat{\boldsymbol{h}}$:

$$\boldsymbol{f}^{inv} * \boldsymbol{f} \approx \delta(n-i) \begin{cases} \approx 1 & \text{if } i = \frac{N+1}{2} \\ \approx 0 & \text{otherwise} \end{cases} \tag{3.19}$$

Now the impulse response can be reconstructed using the start point i and the theoretical sample length of the impulse response Q. It is also found that the position d of the of the actual pulse in the force window (figure 3.3a) is independent of the position of i. This is due to the symmetric auto correlation matrix.

3.4 Auto-correlation matrix

The auto-correlation of a noisy experimental imperfect impulse provides a better signal to noise ratio for detecting dominant frequency components compared to the original force function [6]. In order to find the dominant frequencies in the auto-correlation vector, a Fourier transform is required:

$$\boldsymbol{r}(t) = \int_{\tau=-\infty}^{\infty} \boldsymbol{f}(\tau)\boldsymbol{f}(t+\tau)\, d\tau \tag{3.20}$$

$$\mathcal{F}[\boldsymbol{r}(t)] = \int_{t=-\infty}^{\infty} e^{-j\omega t} \left(\int_{\tau=-\infty}^{\infty} \boldsymbol{f}(\tau)\boldsymbol{f}(t+\tau)\, d\tau \right) dt \tag{3.21}$$

$$= \int_{\tau=-\infty}^{\infty} \boldsymbol{f}(\tau) \left(\int_{t=-\infty}^{\infty} \boldsymbol{f}(t+\tau) e^{-j\omega t}\, dt \right) d\tau \tag{3.22}$$

The Fourier transform of $\boldsymbol{f}(t+\tau)$ is $\boldsymbol{F}(\omega)e^{j\omega\tau}$. Therefore,

$$\mathcal{F}[\boldsymbol{r}(t)] = \boldsymbol{F}(\omega) \int_{\tau=-\infty}^{\infty} \boldsymbol{f}(\tau) e^{j\omega\tau}\, d\tau = \boldsymbol{F}(\omega)\boldsymbol{F}(-\omega) = |\boldsymbol{F}(\omega)|^2 \tag{3.23}$$

Equation (3.23) shows that the Fourier transform of the auto-correlation function is equal to the *auto power spectral density*. The auto-correlation matrix $\boldsymbol{R}$ is decomposed into it's eigenvalues

and eigenvectors to display the same information as the power spectral density in the time domain. The eigenvalues represent the amount of energy and the corresponding eigenvectors the spectral distribution of this energy.

A perfect unit impulse will result in a dense set of frequencies. In order to accurately describe the impact response of a component, the selection criteria of the excitation signal is the power density across the entire bandwidth. The energy density is found if matrix $\boldsymbol{R}$ is diagonalised using a sequence

$$\lambda_1(\boldsymbol{R}) \geqslant \cdots \geqslant \lambda_Q(\boldsymbol{R}) \tag{3.24}$$

of Q real eigenvalues, together with an orthonormal basis of eigenvectors $\boldsymbol{v}_1(\boldsymbol{R}), \ldots, \boldsymbol{v}_Q(\boldsymbol{R})$. The spectral distribution of each eigenvalue is shown in figure 3.4. It is seen that the smallest energy

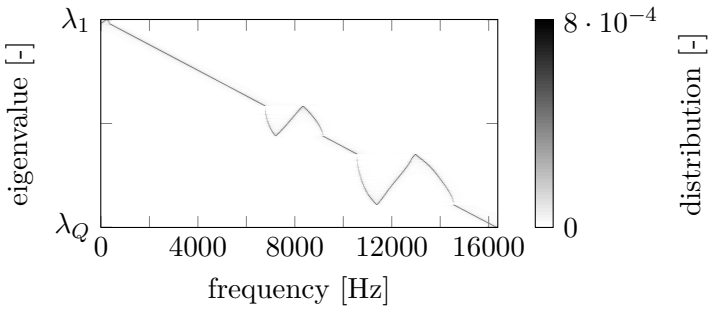

Figure 3.4: *The eigenvalues as a function of the eigenvectors spectral distribution.*

eigenvalue corresponds to the eigenvector with the highest fundamental frequency, which is in good agreement with the power spectral density of an imperfect impulse (see figure 3.5b). The diagonal line from λ_1 at 0 Hz to λ_Q at 1.6×10^4 Hz is interrupted by multiple 'z' shape patterns. In these regions, the eigenvectors contain multiple fundamental frequencies and therefore the eigenvalue will also see this distribution.

The energy density of the eigenvalues are shown in figure 3.5a, by plotting the magnitude of each eigenvalue. The eigenvalue time domain data shows a non-linear behaviour with some similar behaviour to the auto power spectral density in the frequency domain. The two signals are superimposed in figure 3.5c. This similar behaviour can be converted to *exact* behaviour in the linear regions of the eigenvectors spectral distribution of figure 3.4. The eigenvalues of a non-perfect impact can therefore be used as a selection criteria between the replicate measurements.

The power spectral density can again be constructed using the eigenvalues and eigenvectors

$$\mathcal{F}[\boldsymbol{r}(t)] = |\boldsymbol{F}(\omega)|^2 = \mathcal{F}[\boldsymbol{V}\boldsymbol{\Lambda}\boldsymbol{V}^T\boldsymbol{\delta}] \tag{3.25}$$

where the symmetric unit impulse $\boldsymbol{\delta}$ of equation (3.8) was used. This means that the transpose eigenvector matrix is reduced to only the middle column, in order to reconstruct the auto-correlation vector.

3.4.1 Signal separation

The interesting relation between the eigenvalues of the auto correlation matrix and the frequency bandwidth, found in section 3.4, allows for the design of a filter right into the deconvolution operation. The end result: a filtered impulse response, which contains the desired frequency components and the attenuated unwanted frequency components.

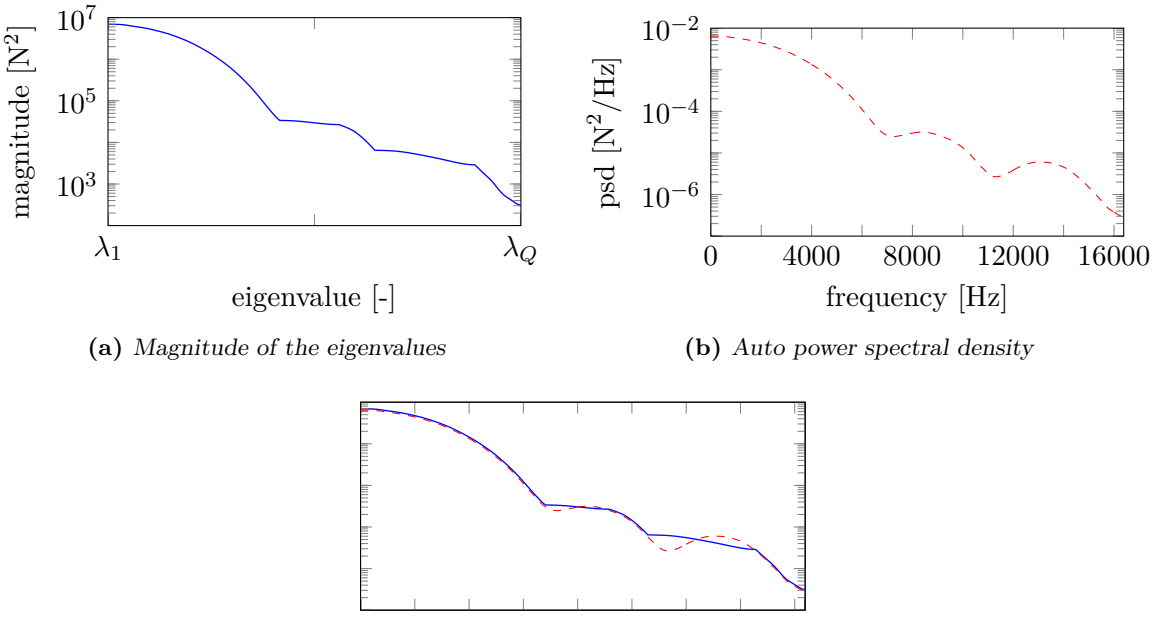

(a) *Magnitude of the eigenvalues*

(b) *Auto power spectral density*

(c) *Superposition of the eigenvalues and the auto power spectral density*

Figure 3.5: *The magnitude of the eigenvalues and the power spectral density of a non-perfect impact.*

The shape of the auto power spectral density of the impact force shows that not all frequencies are excited with the same amount of energy. Consequently, there is a region of frequencies that receives a small amount of energy. In these regions, the output signal shows a increased signal to noise ratio. The deconvolution operation will strongly amplify the magnitude of the higher frequencies to come to a constant energy level. This means that also the noise will be amplified. A filtered experimental impulse response is needed in the region where the energy level is assumed to be constant. This in order to not amplify the uncertainties in the high frequency region.

In order to find the impulse response in the region with assumed constant energy, the time domain data is converted to the frequency domain, the signal is low-pass filtered and the filtered impulse response is found after the inverse Fourier transform. A more direct approach can be presented since the cutoff frequency f_c of a low or high-pass filter can be linked to a single eigenvalue λ_{f_c} in the linear region of the eigenvectors spectral distribution (see figure 3.4).

Using the singular value decomposition the pseudo-inverse of the auto correlation matrix can be easily computed as follows. Let $\boldsymbol{R}$ be decomposed into $\boldsymbol{V}\boldsymbol{\Lambda}\boldsymbol{V}^T$, then

$$\boldsymbol{R}^\dagger = \boldsymbol{V}\Lambda^\dagger\boldsymbol{V}^T \tag{3.26}$$

where the matrix $\Lambda^\dagger$ takes the form:

$$\Lambda^\dagger = \begin{bmatrix} \frac{1}{\lambda_1} & 0 & \cdots & 0 \\ 0 & \frac{1}{\lambda_2} & \cdots & 0 \\ \vdots & \vdots & \cdots & \vdots \\ 0 & 0 & \cdots & \frac{1}{\lambda_Q} \end{bmatrix} \tag{3.27}$$

for all of the non-zero singular values. If any of the λ_i are zero or assumed zero, then a zero is placed in corresponding entry of $\Lambda^\dagger$. If the amplitude of the eigenvalue corresponding to the

cutoff frequency is used as a tolerance for the pseudo inverse of the auto correlation matrix, the least squares minimum norm is found for a filtered impulse response.

For a low-pass filter, all eigenvalues higher or equal to the eigenvalue of f_s will be tolerated in the pseudo inverse. As an example, the non-perfect impact of figure 3.5 is considered and the inverse filter is defined using $\boldsymbol{R}^{\dagger}$. The filtered and original impulse response and it's spectral representation are show in figure 3.6.

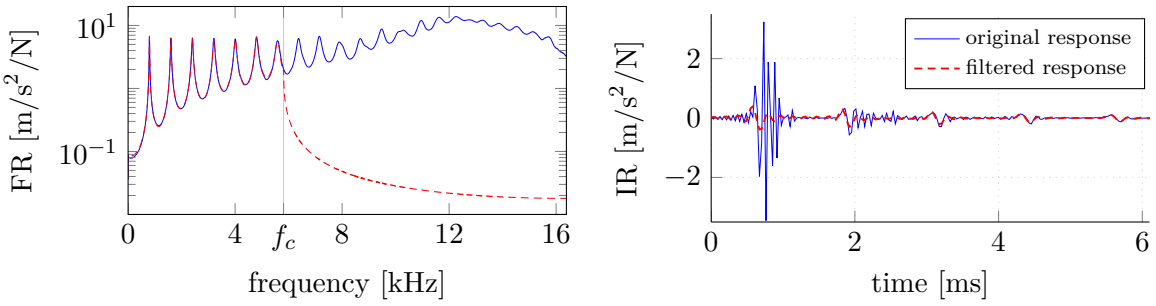

(a) *Frequency response* **(b)** *Impulse response*

Figure 3.6: *The original and low-pass filtered frequency and impulse response. The cutoff frequency f_c at the vertical gray line.*

Figure 3.6a shows that the low frequency signals are passed and are a close match to the original signal. It is also seen that the frequencies higher than the cutoff frequency are attenuated. The filtered impulse response in figure 3.6b skips the high frequency oscillations in the first four milliseconds of the response. After this period a more smoothed signal is seen due to the attenuated high frequency noise.

3.5 Time domain averaging

All experimental data is imperfect and the goals is to minimize errors. The systematic error will stay unknown, but the random error is minimized by doing several replicate measurements and taking the average. In our case performing several impacts to the system and measuring the output. The signal to noise ratio will be increased, theoretically in proportion to the square root of the number of measurements.

3.5.1 Response function estimators

The impulse response function estimator of equation (3.5) is given by the convolution of the inverse filter with the output response. The response function estimation in the frequency domain is more well-known and is derived in a similar manner. The most common approach for the estimation of frequency response functions is also by use of least squares techniques. The algorithms referred to as the $\boldsymbol{H}_1$ and $\boldsymbol{H}_2$ estimators are used based on the assumed location of the noise entering the estimation process [1]. Next the $\boldsymbol{H}_1$ estimator will be given and the direct link to the time domain inverse filter deconvolution:

$$\boldsymbol{H}_1(\omega) = \frac{\boldsymbol{G}_{fu}(\omega)}{\boldsymbol{G}_{ff}(\omega)} \quad \overset{\text{DFT}}{\Longleftrightarrow} \quad \boldsymbol{h}(t) = \boldsymbol{R}^{-1}(t)\boldsymbol{F}^T(t)\boldsymbol{u}(t) \tag{3.28}$$

The cross-power spectral density matrix $\boldsymbol{G}_{fu}(\omega)$ is equal to $\boldsymbol{F}^T(t)\boldsymbol{u}(t)$ since the transpose of the Toeplitz matrix multiplied with any vector produces the linear cross correlation. The auto-power spectral density matrix $\boldsymbol{G}_{ff}(\omega)$ of the force signal is stored in the time domain equivalent

auto correlation matrix $\boldsymbol{R}$, as shown in section 3.4. This means that the impulse response function estimation assumed that the location of noise is on the output response. By taking several replicate measurements and finding the average, the noise on the output is minimised. The $\boldsymbol{H}_2$ estimator and the coherence function will not be given since a time domain equivalent can not directly be found in the deconvolution definition presented here.

3.5.2 Multiple input IRF estimation

The replicate measurements minimise the error on the output response and will be used in the time domain averaging. Section 3.5.1 showed that the time domain deconvolution is equivalent to the $\boldsymbol{H}_1$ estimator, which for multiple inputs is defined as:

$$\boldsymbol{H}_1(\omega) = \frac{1/N_{avg} \sum_{i=1}^{N_{avg}} \boldsymbol{G}_{fu}^i(\omega)}{1/N_{avg} \sum_{i=1}^{N_{avg}} \boldsymbol{G}_{ff}^i(\omega)} \tag{3.29}$$

Note that one over the number of averages can be divided out of equation (3.29) and the cross and auto correlations needs to be calculated for every measurement.

The multiple input impulse response estimation suggested here will again make use of the Toeplitz matrix, but will now be used for storing multiple force inputs $\boldsymbol{F}_{avg}$. The next example gives the time domain averaging for two ($^i = 1, 2$) measurements

$$\begin{bmatrix} u^1[1] \\ u^1[2] \\ \vdots \\ u^1[N] \\ \hline u^2[1] \\ u^2[2] \\ \vdots \\ u^2[N] \end{bmatrix} = \left[\begin{array}{cccc} f^1[1] & 0 & \cdots & 0 \\ \vdots & f^1[1] & & \vdots \\ f^1[M] & \vdots & \ddots & 0 \\ 0 & f^1[M] & & f^1[1] \\ \vdots & & \ddots & \vdots \\ 0 & \cdots & 0 & f^1[M] \\ \hline f^2[1] & 0 & \cdots & 0 \\ \vdots & f^2[1] & & \vdots \\ f^2[M] & \vdots & \ddots & 0 \\ 0 & f^2[M] & & f^2[1] \\ \vdots & & \ddots & \vdots \\ 0 & \cdots & 0 & f^2[M] \end{array}\right] \begin{bmatrix} h_1 \\ h_2 \\ \vdots \\ h_{N-M+1} \end{bmatrix} \Delta t \tag{3.30}$$

Again the least squares minimum norm will be used in finding the impulse response. The auto correlation matrix for multiple input forces is defined as

$$\boldsymbol{R}_{avg} = \boldsymbol{F}_{avg}^T \boldsymbol{F}_{avg} = \sum_{i=1}^{N_{avg}} \boldsymbol{R}^i \tag{3.31}$$

The energy densities, as show in section 3.4, will be stores in the auto correlation vector but now for the averaged impact. The conditioning of the averaged auto correlation matrix will determine the accuracy of the inverse filter and it's therefore interesting to see how this number is influenced by the sum of the auto correlation matrices.

Eigenvalues The eigenvalues of the sum $\boldsymbol{R}^1 + \boldsymbol{R}^2$ of two Hermitian Q by Q matrices can be written in terms of the eigenvalues of $\boldsymbol{R}^1$ and $\boldsymbol{R}^2$. The eigenvalues are bounded by the inequalities [16]

$$\lambda(\boldsymbol{R}^1 + \boldsymbol{R}^2)_{k+l-1} \leqslant \lambda(\boldsymbol{R}^1)_k + \lambda(\boldsymbol{R}^2)_l \qquad \text{for } k + l - 1 \leqslant Q \tag{3.32}$$

The biggest eigenvalue of $\boldsymbol{R}^1 + \boldsymbol{R}^2$ is bounded by one inequality: $\lambda(\boldsymbol{R}^1 + \boldsymbol{R}^2)_1 \leqslant \lambda(\boldsymbol{R}^1)_1 + \lambda(\boldsymbol{R}^2)_1$, whereas the following sum of eigenvalues is bounded by an increasing amount of inequalities. Since the condition number depends on the first and last eigenvalue: $\lambda(\boldsymbol{R}^1+\boldsymbol{R}^2)_Q \geqslant \lambda(\boldsymbol{R}^1)_Q+\lambda(\boldsymbol{R}^2)_Q$, the condition number decreases more beneficial than the linear combination of the separate eigenvalues could suggest. This means that a replicate measurement with a large condition number can also be included into the averaging process without sacrificing on the accuracy.

The most costly operation is taking the inverse of the auto correlation matrix. In this averaging method, the inverse autocorrelation matrix is only calculated once and has the same size as the auto correlation matrix of a single input force. Now the inverse filters are found when the inverse averaged auto correlation is correlated with the reversed single force pulses

$$\boldsymbol{f}_i^{inv} = \boldsymbol{R}_{avg}^{-1} \boldsymbol{F}_i^T \boldsymbol{\delta} \tag{3.33}$$

The impulse response reconstruction of multiple replicate measurements is estimated by the summation of the inverse force filters convolved with the corresponding output responses $\boldsymbol{u}^i$

$$\boldsymbol{h}_{avg} = \sum_{i=1}^{N_{avg}} \boldsymbol{f}_i^{inv} * \boldsymbol{u}^i \tag{3.34}$$

If the time domain IRF estimation of equation (3.34) is compared to the FRF estimator of equation (3.29), it is seen that the factor $1/N_{avg}$ is divided out of the equation in the spectral representation and in the time domain this factor is found back in the inverse averaged auto correlation vector. A difference between the two equations is that the auto correlation in the time domain is only calculated once, whereas the spectral estimation needs to calculate the auto correlation for every replicate measurement. The time-domain method is compared to that of the frequency domain estimator in figure A.1. A perfect match is found for both the amplitude and phase.

3.6 Method validation

The accuracy and the computational time depend on two variables. In this section the sensitivity to these variables will be determined.

The Condition number of the auto-correlation matrix $\boldsymbol{R}$ is given by the ratio between the biggest and lowest eigenvalue. The condition number for an unit impulse will be equal to one, which means that its inverse necessary for finding the inverse FIR filter can be computed with good accuracy. If the condition number is large, then the matrix is said to be ill-conditioned. Practically, such a matrix is almost singular, and the computation of its inverse, or solution of a linear system of equations is prone to large numerical errors. A matrix that is not invertible has the condition number equal to infinity. An example to a non invertible auto-correlation matrix would be a sinusoidal force function of a single frequency.

The condition number of three experimentally obtain impulses is show in figure 3.7a as a function of the output sample length. It is observed that the condition number reaches an upper bound, which means that the additional information in the autocorrelation matrix does not contribute to a more accurate calculation of the eigenvalues. If the replicate measurement with the lowest condition number is found in the accuracy plot of figure 3.7b, it is seen that a correlation matrix with the lowest condition number results in the inverse force filter with the best accuracy.

As shown in section 3.4, the eigenvalues represent the amount of energy and the eigenvector determines the distribution of the energy. If the point of observation is the frequency domain, the ratio between the highest and lowest value of the auto power spectral density will give a good estimate for the condition number of $\boldsymbol{R}$.

The accuracy of the inverse filter also depends on the dimensions of the Toeplitz matrix. The accuracy is defined as the absolute length of the samples that construct the unit impulse. Because the theoretical value should be equal to one, this number is also subtracted from this vale in order to graphically show the accuracy in figure 3.7b. The solid lines represent the accuracy check for time-domain acquired inverse force filters and the dashed lines represent the inverse filter found by frequency domain operations. The inverse filters in the frequency domain are found by the following operation IDFT[1./DFT[$\boldsymbol{f}(t)$]] and is graphically shown in figure 3.8.

It is observed that the frequency domain gives an more accurate inverse filter. There are more calculations required for the time-domain approach, which gives more round off errors, compared to that of the frequency domain method. For every force filter there will be an optimum sample length N. The inverse filter will gradually get more accurate as the output length increases and find an optimum between the region of lack of information in the auto-correlation matrix and the region where the round-off errors are dominant.

The computational time is calculated as a function of the inverse filter length. Although speed optimisations are not in the context of this thesis, for completeness the comparison is made between the frequency and time-domain acquired inverse force filter. The results are shown in figure 3.7c. It is seen that the time-domain approach is at less time efficient (optimisations in the calculations, shown in appendix A.1, can lead to better time efficiency).

3.7 Summary

Time-domain deconvolution is possible by defining an inverse FIR force filter which is independent of the output response. This inverse filter is convolved with the output response in order to obtain the impulse response function. The eigenvalue decomposition of the correlation matrix makes choosing between replicate measurement and signal filtering possible. Averaging of multiplicative measurements in time domain is possible and is equivalent to the frequency domain $\boldsymbol{H}_1$ estimator. The accuracy of the inverse filter is sensitive to the conditioning of the auto-correlation matrix and the inverse filter length. Due to more computations, the time-domain approach is less accurate and less time efficient compared to that of the frequency domain acquired inverse filter. For a better understanding of the inverse force filter, a comparison is made between the two operational domains in figure 3.8.

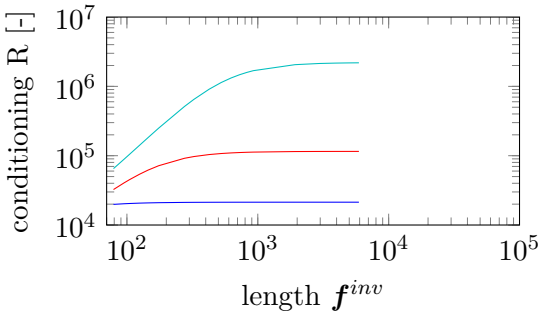

(a) *Conditioning of auto-correlation matrix* $\boldsymbol{R}$ *as a function of the inverse filter length*

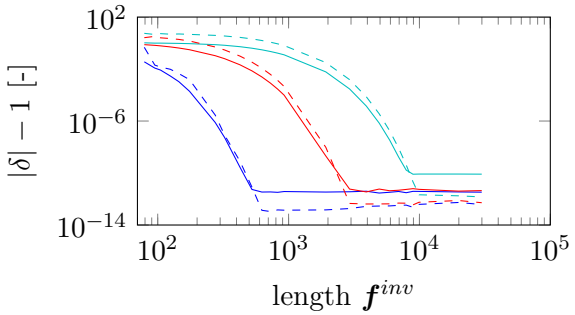

(b) *The accuracy of the inverse FIR filter shown as a function of the inverse filter length*

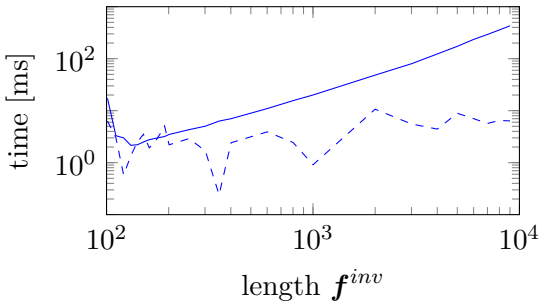

(c) *Computational time as a function of the inverse filter length*

Figure 3.7: *Sensitivity analysis on the accuracy of the time-domain inverse FIR filter (solid lines), for three experimentally obtained impacts. The dashed lines are inverse force filters found through the frequency domain.*

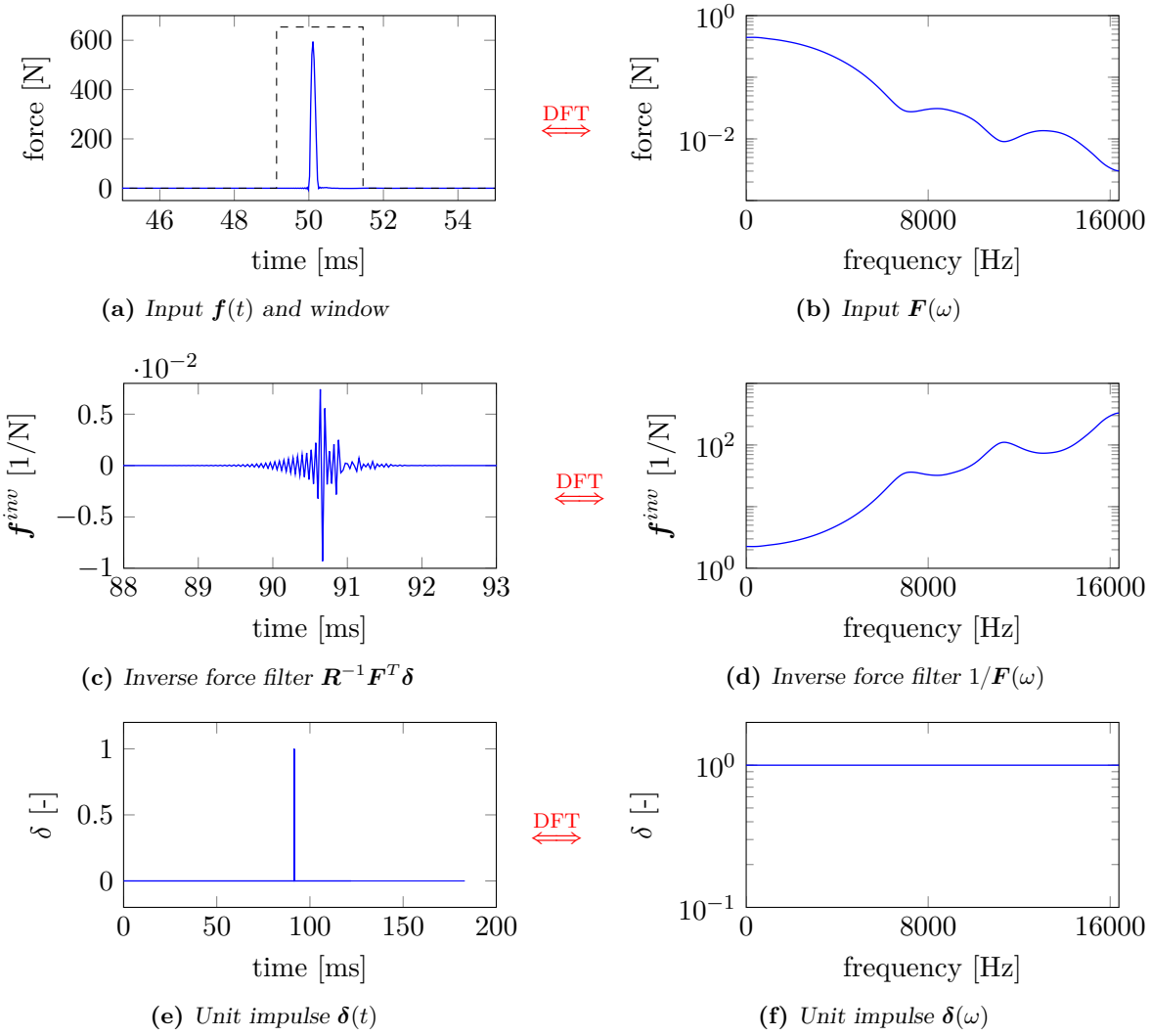

(a) *Input* $\boldsymbol{f}(t)$ *and window*

(b) *Input* $\boldsymbol{F}(\omega)$

(c) *Inverse force filter* $\boldsymbol{R}^{-1}\boldsymbol{F}^{T}\boldsymbol{\delta}$

(d) *Inverse force filter* $1/\boldsymbol{F}(\omega)$

(e) *Unit impulse* $\boldsymbol{\delta}(t)$

(f) *Unit impulse* $\boldsymbol{\delta}(\omega)$

Figure 3.8: *Determination of the inverse force filter and the accuracy check in the time (left) and frequency domain (right).*

Chapter 4

Dynamic substructuring using impulse response functions

4.1 Introduction

Now that the impulse response functions are calculated, the theory behind the impulse based substructuring scheme is presented. The dynamics of the substructures will be coupled, such that the dynamics of the total structure is found. This is done by introducing the interface probem. The numerically simulated and experimental obtained impulse response functions will be tested in the dynamic substructuring scheme for stability and compatibility.

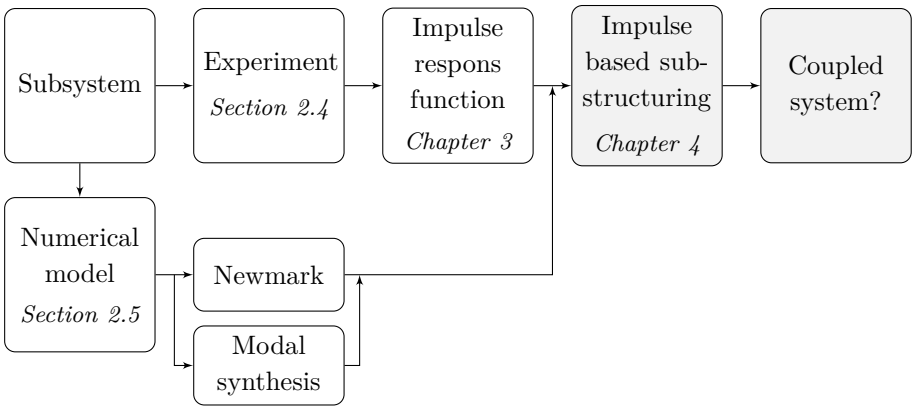

Figure 4.1: *Overview and subjects addressed in this chapter in gray.*

4.2 Impulse based substructuring

In this section the dynamics of structures will be coupled by means of the impulse responses. In order to assemble the interface degrees of freedom of the substructures, two conditions need to be satisfied:

Compatibility is accieved when two matching interface degrees of freedom have the same displacements and rotations, i.e., $\boldsymbol{u}_i^{(1)} = \boldsymbol{u}_i^{(2)}$, where the subscript i denotes the interface degrees of freedom. The compatibility condition for the full set of DoF can be elegantely

written using the signed Boolean matrix $\boldsymbol{B}$, which selects the substructures interface DoF

$$\sum_{s=1}^{N^s} \boldsymbol{B}^{(s)} \boldsymbol{u}_n^{(s)} = \boldsymbol{0} \tag{4.1}$$

Note that also compatibility can be claimed for the accelerations and velocities. In section 4.2.1, the interface DoF of the substructures are assumed to have the same velocity.

Equilibrium on the interface DoF is realised when the reaction forces are equal in magnitude and opposite in sign: $\boldsymbol{g}^{(1)} + \boldsymbol{g}^{(2)} = \boldsymbol{0}$. By making use of the same signed Boolean operator from equation (4.1), this condition can be written as:

$$\begin{bmatrix} \boldsymbol{g}^{(1)} \\ \boldsymbol{g}^{(2)} \end{bmatrix} = -\boldsymbol{B}^T \boldsymbol{\lambda}, \tag{4.2}$$

where $\boldsymbol{\lambda}$ are the unknown Lagrange multipliers that must be determined in order to satisfy the compatibility condition. So, the Lagrange multipliers represent the force necessary for keeping the interface DoF connected.

4.2.1 Assembly of impulse responses

The velocity in time for a general applied force $\boldsymbol{f}(t)$ can be found by approximating the convolution integral from equation (2.6) by the finite sum

$$\dot{\boldsymbol{u}}_n^{(s)} = \sum_{i=0}^{n} \dot{\boldsymbol{H}}_{n-i} \left(\boldsymbol{f}_i + \boldsymbol{g}_i \right) \Delta t \tag{4.3}$$

where the subscripts indicate the present time step: $\dot{\boldsymbol{u}}_n = \dot{\boldsymbol{u}}(t_n)$. The sum running from $i = 0$ to n states that $\dot{\boldsymbol{H}}_0$ is non zero, this is also true for the accelerations $\ddot{\boldsymbol{H}}_0$. When the displacements are used for the impulse based substructuring, the impulse response $\boldsymbol{H}_0$ on the first time step is zero and the summation limits can be shortened. The impulse response matrix for our system writes:

$$\dot{\boldsymbol{H}}_n = \begin{bmatrix} \dot{h}_0^{(1)}(n) & \dot{h}_L^{(1)}(n) \\ \dot{h}_L^{(1)}(n) & \dot{h}_0^{(1)}(n) \end{bmatrix} \tag{4.4}$$

Equation (4.3) is not consistent with the Newmark time integration scheme as shown in [12], since it assumes the force to be piecewise linear between t_n and t_{n+1}. If the impulse superposition needs to be consistent with the constant average acceleration Newmark, the impulse responses are averaged and substituted in equation (4.3), as was proposed in [15]:

$$\dot{\hat{\boldsymbol{H}}}_n = \tfrac{1}{2}(\dot{\boldsymbol{H}}_n + \dot{\boldsymbol{H}}_{n+1}) \tag{4.5}$$

Substitution of the equilibrium and compatibility condition, respectively equations (4.1) and (4.2), into the impulse response in terms of velocities of equation (4.3), results in the coupled equations.

$$\left| \begin{array}{l} \dot{\boldsymbol{u}}_n^{(s)} = \Delta t \sum_{i=0}^{n} \dot{\hat{\boldsymbol{H}}}_{n-i}^{(s)} \left(\boldsymbol{f}_i^{(s)} - \boldsymbol{B}^{(s)^T} \lambda_i \right) \\ \sum_{s=1}^{N^s} \boldsymbol{B}^{(s)} \dot{\boldsymbol{u}}_n^{(s)} = \boldsymbol{0} \end{array} \right. \tag{4.6}$$

The Lagrange multipliers $\boldsymbol{\lambda}$ represent the impulse needed for compatibility. By expanding the velocities in time from equation (4.6), it can be quantified into two parts: a known part and an underlined unknown part:

$$\dot{\boldsymbol{u}}_n^{(s)} = \Delta t \sum_{i=0}^{n-1} \dot{\hat{\boldsymbol{H}}}_{n-i}^{(s)} \left(\boldsymbol{f}_i^{(s)} - \boldsymbol{B}^{(s)^T} \boldsymbol{\lambda}_i \right) + \Delta t \, \dot{\hat{\boldsymbol{H}}}_1^{(s)} \boldsymbol{f}_n^{(s)} \underline{- \Delta t \, \dot{\hat{\boldsymbol{H}}}_1^{(s)} \boldsymbol{B}^{(s)^T} \lambda_n} \tag{4.7}$$

A prediction can be made from the known part in equation (4.7), called $\tilde{\boldsymbol{u}}_n^{(s)}$, of the substructures velocities when the interface forces $\boldsymbol{g}_n^{(s)}$ are equal to zero. The total velocities are thus written as

$$\dot{\boldsymbol{u}}_n^{(s)} = \dot{\tilde{\boldsymbol{u}}}_n^{(s)} - \Delta t \, \dot{\hat{\boldsymbol{H}}}_1^{(s)} \boldsymbol{B}^{(s)^T} \lambda_n \tag{4.8}$$

With this prediction on the velocities, the Lagrange multipliers needed to ensure compatibility are calculated by substituting equation (4.8) in the compatibility condition of equation (4.6).

$$\boldsymbol{\lambda}_n = \left(\Delta t \sum_{s=1}^{N^s} \boldsymbol{B}^{(s)} \dot{\hat{\boldsymbol{H}}}_1^{(s)} \boldsymbol{B}^{(s)^T} \right)^{-1} \sum_{s=1}^{N^s} \boldsymbol{B}^{(s)} \dot{\tilde{\boldsymbol{u}}}_n^{(s)} \tag{4.9}$$

The term inside the braces needs to be inverted and can be seen as the effective dynamic stiffness tensor for the interface degrees of freedom. The Lagrange multiplier is the magnitude of the force necessary to keep the substructures together, i.e. the same internal force which is always present between discretised structural elements. Note that solving for the Lagrange multipliers on the interface is similar to the dual interface problem for the frequency based substructure [5]. Finally, a correction on the predicted velocity $\dot{\tilde{\boldsymbol{u}}}_n^{(s)}$ is made by solving equation (4.8). This procedure is repeated for every time step.

4.3 Substructuring with numerical models

The full system is split up into two symmetric numerical models, as introduced in section 1.2.1. The impulse based substructuring scheme will try to ensure that the two substructures together behave in the same way as the numerical full system. Next, the two ways of numerical simulations, described in section 2.5, are tested for stability and compatibility.

4.3.1 Newmark time integration

The impulse response, found if the external excitation is equal to the unit impulse, is proven to be consistent with the impulse based substructuring algorithm [12]. This means that the coupling process is independent of the time step. It will therefore be no surprise that the coupled response is stable and compatibility ensures overlap of the full Newmark simulated response, as shown in figure 4.2a. The inherent periodicity error of the constant average acceleration scheme is equal for the coupled and full simulated response.

4.3.2 Modal synthesis

The modally synthesised impulse response functions of the substructures, as presented in section 2.5.2, are not suitable for the coupling process. The result of the impulse based substructuring scheme with averaging shows a uncoupled stable response, see figure B.1b. From the impulse response function of the substructures, in figure B.1a, it is observed that the magnitude of the extremal values of the waves are underestimated.

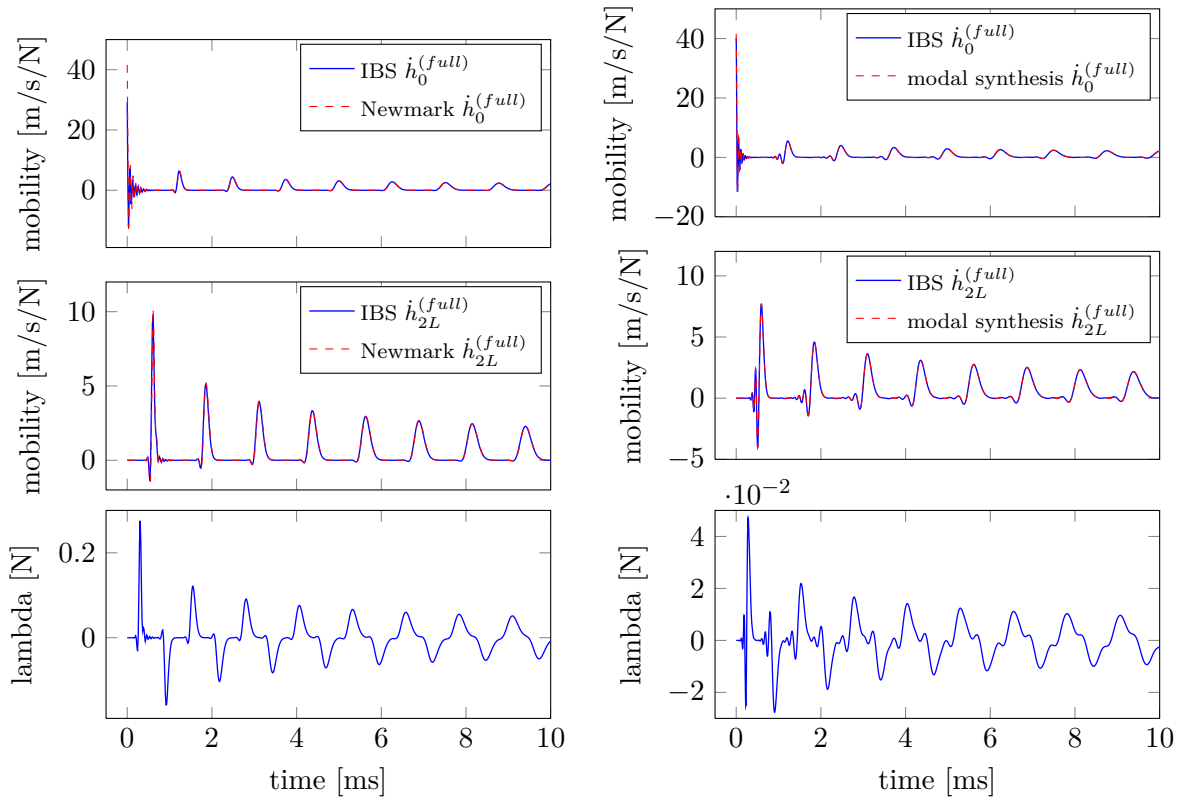

(a) *Coupling and reference Newmark IRF's* **(b)** *Coupling and reference modally synthesised IRF's*

Figure 4.2: *Impulse based substructuring using simulated impulse response functions.*

The transient dynamic substructuring algorithm is proven to be consistent with the Newmark time integration scheme. This implies that the inputs for the coupling process have to be equal to the time integrated responses. This is only the case for time steps which approach zero: $\Delta t \to 0$, in which the Newmark time integrated response converges to the exact modally superimposed solution. The convergence of the Newmark time integration to the analytical solution is sketched in figure 4.3.

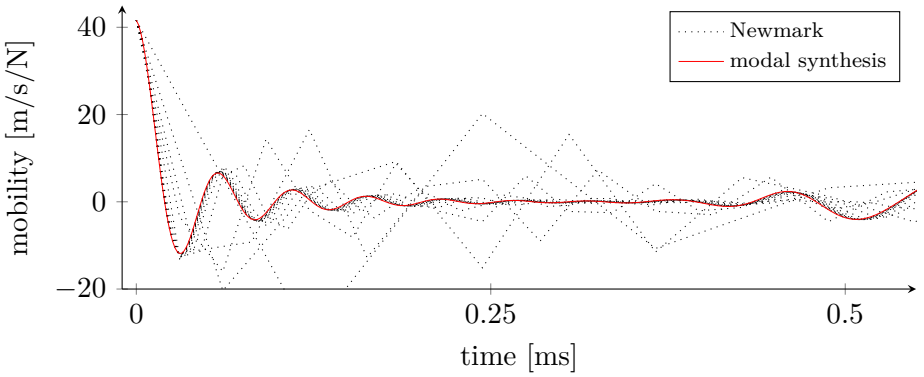

Figure 4.3: *The convergence of Newmark (as a function of the step size) towards the analytical solution.*

If the model is simulated with a time step which is ten times smaller as that of the experiment, the substructuring scheme produces a stable coupled impulse response, as shown in figure 4.2b. The coupled impulse responses are compared to that of the full model, with length equal to $2L$. The results are in good agreement but come at a higher cost. The very small time step makes the algorithm more computationally expensive. Due to the nature of the convolution product, the number of calculations grows quadratically with the number of samples.

4.4 Substructuring with experimental data

The experimentally obtained impulse response functions of the subcomponents are found with the time-domain deconvolution operation, proposed in chapter 3, for 5 replicate measurements and were shown in figure 2.7. The results of the impulse based substructuring scheme together with the measurement of the full system are shown in figure 4.4.

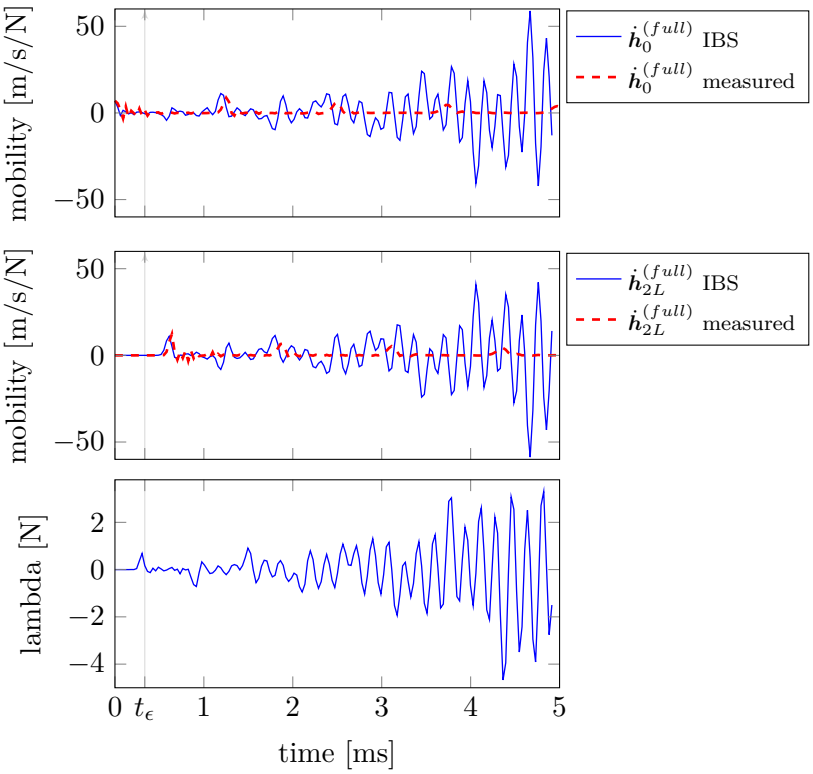

Figure 4.4: *Impulse based substructuring using measured impulse response functions.*

The end face $\dot{\boldsymbol{h}}_{2L}^{(full)}$ shows correct coupling up to the first period, which is at 0.6 ms. The rest of the signal is dominated by instability, which is assumed to start growing at t_ϵ; the first wave of the cross point $\dot{\boldsymbol{h}}_L^{(1)}$. At this instant in time, energy is gained into the system due to increased amplitude of the impulse response compared to the first wave of the driving point $\dot{\boldsymbol{h}}_0^{(1)}$. Chapter 5 will give more detail to this reasoning, when its tried to alter the measured impulse response functions.

4.5 Summary

The impulse response functions resulting from modal superposition will be a downsampled version of the continuous underlying function, similar to that of the measurement. The Newmark time integrated responses will converge to the analytical solution for very small time steps. Since the impulse based substructuring scheme is consistent with the Newmark time integration, only modally superimposed impulse response functions with high sampling rate can be used. This will make the coupling process possible but at a higher cost.

The direct time-domain deconvolved, experimentally obtained, impulse response functions do not lead to a stable coupled system. The coupled results are dominated by instability, which renders them useless.

Chapter 5

Strategies for improving experimental IRF's for dynamic substructuring

5.1 Introduction

The direct time domain deconvolution method did not change the impulse response function in such an extend that dynamic substructuring was feasible, as was shown in section 4.4. Therefore, the flow chart in figure 5.1 does not give the operations necessary to get to the desired result: coupling experimental impulse response function. The problem of why the the coupling does not takes place is unknown and turns this part of the thesis into an exploratory research. Due to the fundamental nature of this research, not all the possible options are investigated. The most feasible options, in the effort of coupling experimental impulse response functions, are presented in this chapter. The system was identified in chapter 2 both experimentally and numerically, in order to spot the immediate difference between the two methods. Insight in these differences gives rise to the formulation of hybrid impulse response functions. The perfect modelled responses are also used to investigate operations which jeopardise the substructuring routine, i.e. filtering, re-sampling and measurement errors. This chapter concludes with an operation that gets rid of some experimental errors introduced into the impulse response.

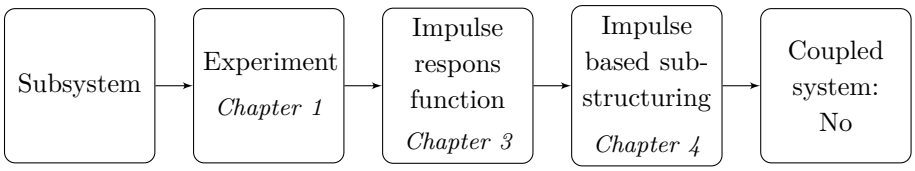

Figure 5.1: *The operations in flowchart do not lead to coupling of experimental impulse response functions.*

5.2 Exploratory research

In contrast to the measured response, both simulated response functions could be successfully used in the coupling process, as shown in chapter 4. In this section the apparent differences between the two worlds of acquiring the impulse response are listed. These differences are labelled as possible problems why no coupling between measured responses takes place or instability

occurs. After the possible problem definition, the measured impulse response can be altered and the sensitivity of the impulse based substructuring scheme be analysed.

- The first sample of the driving point $\dot{\boldsymbol{h}}_0^1$ of the model is eight times larger as the first sample of the measurement (see figures 2.7b and 2.9a). The driving point impulse response suggests that energy is gained during the fist period of the signal, as shown in figure 5.2b, rendering the system non-causal. This first sample is of great importance because its value is used in every time step of the convolution operation, see equation (4.9). The impulse response should start at a maximum after which an exponential decay is seen, since we deal with a non-conservative system. The origin of this problem is observed when examining the output velocity, as shown in figure 5.2a. Due to the non perfect impact, the velocity of the returning wave is of higher amplitude than that of the initial wave. This makes sense when you imagine pushing in a mass-spring system. During the time when the force is applied, potential energy is build up in the spring. When the mass-spring system is released, it will have more velocity returning to the equilibrium position since all the kinetic energy is released.

  Sections of the measured response are replaced with simulated ones in section 5.3 and the sensitivity of the exponential decay of the mobility functions is shown in section 5.4.4.

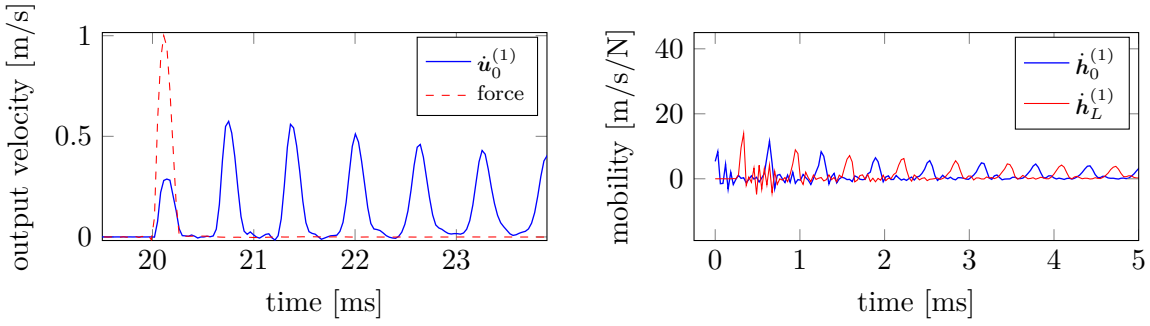

(a) *Output velocity and normalised non perfect impact force on the driving point*

(b) *Errors of the exponential decay in the measured impulse resonse functions*

Figure 5.2: *Defects in the measured output and impulse response.*

- The simulated response functions are without any noise. The influence of noise will be examined in section 5.4.1

- The measurement and simulations all have different sampling rates. This makes it difficult to create a hybrid model. The effects of re-sampling and filtering are shown in section 5.4.2.

- The inherent periodicity error $\omega^2 h^2/12$ of the Newmark constant acceleration scheme is seen back in the comparison with the measurement and the modally synthesised response. This error will not be examined further because the measurement is, like the modal synthesised response, a down-sampled version of the underlying continuous function.

- Compared to simulations, the measurement shows more dynamics in the high frequency region. The frequency response functions in figure 2.6 also shows that the dynamics in this region are not in good agreement. The effect of different underlying high frequency dynamics is worked out in section 5.4.3

- The rigid body motion in the measurement is shifted to approximately 7 Hz due to the suspension of the experimental setup, see figures 2.7a, 2.7c, 2.9a and 2.9c. This low frequent oscillation is not seen back in the simulations. This is investigated in section 5.4.3

5.3 Hybrid substructuring

The measured impulse response of the substructures are partially replaced with simulated data before the coupling process and is called hybrid substructuring. The first point of the impulse response of the driving point $\dot{\boldsymbol{h}}_0^{(1)}(1)$ is replaced with that of the numerical model. In order to see what happens to the Lagrange multiplier, equation (4.9) is recalled:

$$\boldsymbol{\lambda}_n = \left(\Delta t \sum_{s=1}^{N^s} \boldsymbol{B}^{(s)} \dot{\boldsymbol{H}}_1^{(s)} \boldsymbol{B}^{(s)^T} \right)^{-1} \sum_{s=1}^{N^s} \boldsymbol{B}^{(s)} \tilde{\dot{\boldsymbol{u}}}_n^{(s)}$$

If the magnitude of the first point of the driving point is to large, the Lagrange multiplier is underestimated meaning that there is too little force to keep the substructures together. This will result in an uncoupled response. If the denominator is to small, the force is overestimated, resulting in instability in the impulse based substructuring scheme.

The result of the hybrid substructuring is shown in figure 5.3. The blue line is a stable but uncoupled response and has the first driving point value of the simulation. Next, this value is gradually lowered, resulting in increasingly unstable behaviour. The transition point between the uncoupled response and unstable behaviour is not equal to the desired coupled response.

Replacing the entire driving point impulse response or shorter sections with numerical data also leads to an uncoupled or unstable response, depending on the length of the copied section.

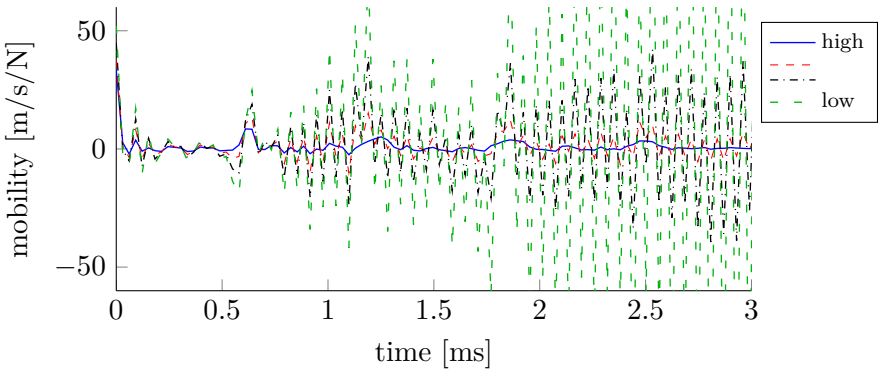

Figure 5.3: *The response after substructuring of point $\dot{\boldsymbol{h}}_0^{(full)}$ to investigate the sensitivity of the first driving point $\dot{\boldsymbol{h}}_0^{(1)}(1)$. The highest value results in the uncoupled response. Gradually lowering this value gives an unstable and uncoupled response.*

5.4 Substructuring sensitivity analysis

The methodology for evaluation of the effects of the measurement imperfections is as follows: the imperfections of the measurement are represented with numerical models to see their sensitivity to the impulse based substructuring scheme.

5.4.1 Influence of noise

The influence of noise on the coupling of the impulse responses is examined by introducing noise in the deconvolution operation. It is said that measurement noise has a blurring effect on the evolution of dynamical systems, which can be seen in figure 2.6. Modelling the precise effects of noise on a dynamical system can be very difficult, especially the high frequency part. It can involve a lot of guesswork because the exact measure of the noise is not known. However, one can already gain insight into the effect of noise on a system by adding Gaussian white noise. This noise is a mathematical construct that approximates the properties of many kinds of noise encountered in experimental situations.

As a basis, the impulse responses of a Newmark simulation with constant average acceleration is used. The influence of noise on the output signal will be examined, as is done in the experimental case for the H_1 estimator (see section 3.5.1). The 'perfect' impulse is convolved with an experimental impact force, resulting in the output response, according to the following formula:

$$\boldsymbol{f}(t) * \boldsymbol{h}(t)\, \Delta t = \boldsymbol{u}(t) + \boldsymbol{\zeta}(t) \tag{5.1}$$

where the added white Gaussian noise is represented by $\boldsymbol{\zeta}(t)$. Now the direct time-domain deconvolution finds the impulse response corresponding to the input force and the noisy output response. This impulse response is than used as the input to the coupling process. With the introduction of the noise on the output, two extrema test cases can be constructed:

No noise on the output signal ($\boldsymbol{\zeta}$(t)=0). The impulse response is now only contaminated with numerical noise due to the convolution with the force and the deconvolution with the inverse force filter. The impulse responses are coupled and the result show in figure 5.4b as the solid line, were a correct coupled response is found with double the period time between the running waves, compared to that of the symmetric substructure. Also the compatibility condition of equation (4.1) is examined for amplitude and stability. Figure 5.4c shows the difference between the two interface degrees of freedom $\left|\ddot{\boldsymbol{u}}_L^{(1)} - \ddot{\boldsymbol{u}}_0^{(2)}\right|$. The maximum absolute acceleration gap between the two interface degrees of freedom is $0.25\,\mathrm{pm/(s^2\,N)}$ and a decaying to a constant numerical error is observed.

Next to the test case described in equation (5.1), the non perfect impact $\boldsymbol{f}(t)$ was also used as the external excitation in the Newmark time integration scheme. The output response was convolved with the inverse force filter, resulting in the impulse response. After dynamic substructuring, this also resulted in perfectly coupled full system responses.

Maximum noise is introduced on the output signal until the moment that the coupled system shows some sign of instability. The power of the output response is measured in decibel watt and the signal-to-noise ratio is set to 27 dB. The result is shown in figure 5.4a as the dashed line. The magnitude of the compatibility condition is in the same order of magnitude as the case were no noise was applied but the signal shows a growth in acceleration difference around 10 ms, rendering the coupling unstable. Note that the same instability result can be found in the Lagrange multiplier. The coupled full system response in figure 5.4b starts to decouple, seen by the small wave in between the running waves.

5.4.2 Re-sampling and filtering

If the measurement is similar to that of the modally synthesised impulse response, due to the underlying continuum response, the measurement needs to be up-sampled in order for the

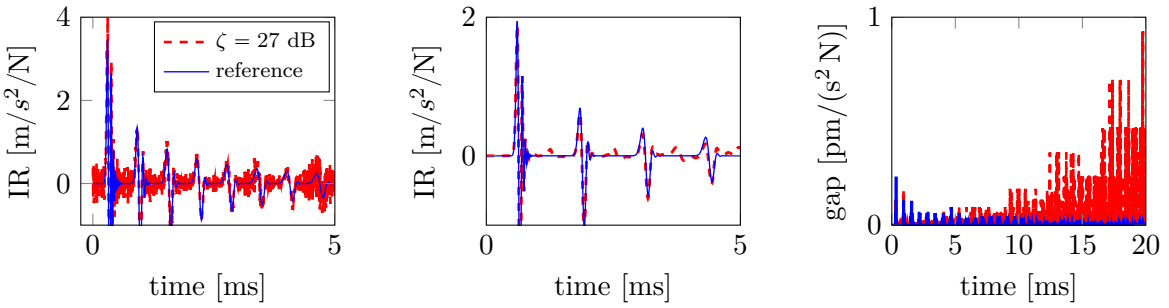

(a) *Impulse response* $\ddot{\boldsymbol{h}}_L^{(1)}$ *of substructure. The solid line the noise due to deconvolution and the dashed line the added white Gaussian noise.*

(b) *Impulse response* $\ddot{\boldsymbol{h}}_{2L}^{(full)}$ *of full model after impulse based substructuring.*

(c) *The absolute acceleration difference between the interface degrees of freedom.*

Figure 5.4: *The input, output and the gap between the substructures of the dynamic substructuring process when noise is added.*

impulse based substructuring scheme to work. It is possible for the modal superimposed result of the substructures to be re-sampled before acquiring the coupled response. The same attempt on the measurement failed due to the inclusion of measurement noise on the signal.

A possibility for finding cleaner impulse response functions is by applying a low pass filter. This will get rid of the high frequency noise and mismatching dynamics. There are again two ways of filtering the system, a time-domain approach as proposed in section 3.4.1 and in the frequency main with a Butterworth filter [3]. The filtering process was tested on simulated responses. Dynamic substructuring after the responses of the substructures were filtered led to instability in the results. The filtering process has a big influence on the first point of the driving point, such that no fluent exponential decay is spotted in the impulse response functions of the substructures.

5.4.3 Change underlying dynamics

In order to see the influence of the mismatching high frequency dynamics, as was seen for the measured substructures (figure 2.6), a numerical model will be tuned. The modal parameters of the perfect simulation are altered to give a different impulse response for one of the interface degrees of freedom. The cross point $\dot{\boldsymbol{h}}_L^{(1)}$ is the modelled response and the driving point $\dot{\boldsymbol{h}}_0^{(1)}$ is altered. The high frequency response, after 9 kHz, now contains different eigenfrequencies and damping parameters. The frequency response function is shown in figure 5.6a, where the dotted black line is changed into the red dashed line. The effects in the transient response is shown in figure 5.5a. It clearly shows different high frequency dynamics in the beginning of the signal as long as the damping ratio allows.

The substructures with mismatching underlying dynamics are now tested in the impulse based substructuring scheme. The result is presented in figure 5.5b. The substructured response does not show perfect coupling during the first period of the signal (the red dashed line). The introduced error has however no influence on the remaining response. This is remarkable, since the Lagrange multipliers ensuring compatibility in the first period are also used in the proceeding calculations of the convolution operation. The error is not big enough for creating an immediate unstable behaviour. As the error is quickly damped out, due to the high frequency damping ratio, also does the error on the Lagrange multiplier.

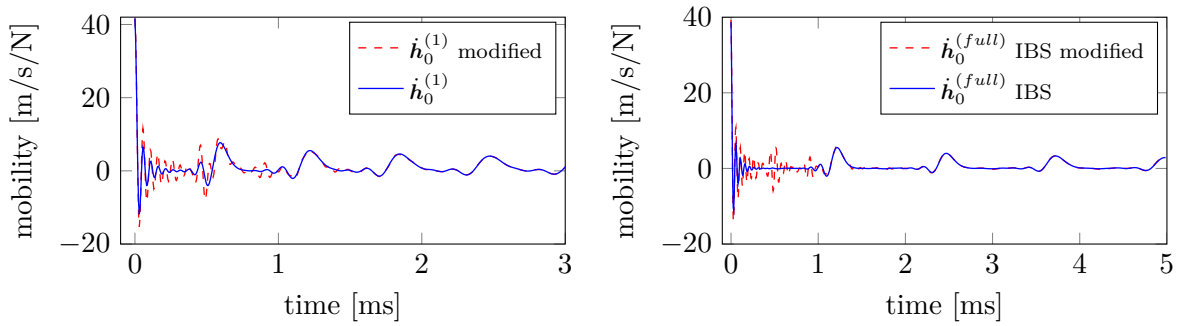

(a) *Changed high frequency of subcomponsent*

(b) *IBS of perfect and coupled response with changed high frequency dynamics of driving point subcomponent*

Figure 5.5: *Only the high frequency characteristics of the driving point are altered, after which the impulse based substructuring scheme is conducted.*

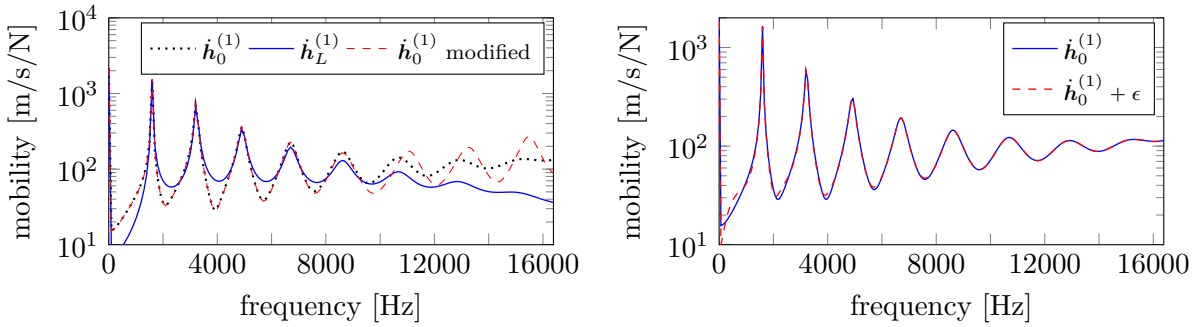

(a) *Changed high frequency dynamics*

(b) *Amplitude error*

Figure 5.6: *Frequency response functions of the driving point where first the dynamics and later the amplitude is changed.*

The same procedure was also followed by shifting the rigid body mode to a higher frequency, but mismatching for the two interface degrees of freedom. Again a stable and coupled response was observed.

5.4.4 Exponential decay

The simulated data shows constant exponential delay in the impulse response functions. Figure 5.2b shows that this is not at all the case for the measurement. No exponential function can be plotted through the peak of the waves. Four obvious points are picked at time p_1 to p_4 in this figure. The non perfect impact is the cause for the amplitude error of peak p_1. Measurement induced errors such as small differences in the frequency of the rigid body mode and discretisation error can be the cause for the amplitude error of peak p_3.

This problem is again simulated using numerical data. At time t_ϵ an error is introduced into the impulse response function. The simulation is shown in figure 5.7a, where the dotted black line is the perfect response and the solid blue line containing the small amplitude error. The error in this example is $\epsilon = 5\%$, but the same behaviour also occurs for an error of less than one percent. The impulse response functions are now coupled and shown in figure 5.7b. An amplitude error on the second (or any) period will decouple the subsystems. If the change

in amplitude is small, the compatibility error starts to accumulate and will cause complete decoupling after several periods.

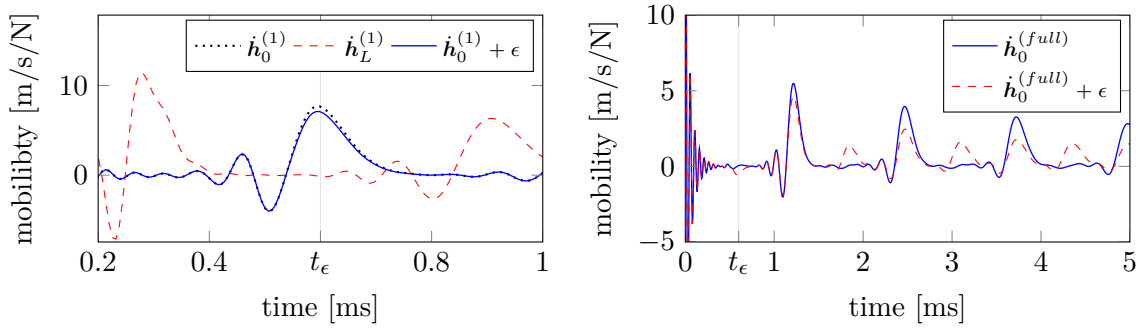

(a) *Small amplitude error on* $\dot{\boldsymbol{h}}_0^{(1)}$

(b) *Perfect IBS and uncoupled response*

Figure 5.7: *A small amplitude error on the impulse response of the substructure results in an uncoupled response.*

The influence of the amplitude error on the spectral part of the data is shown in figure 5.6b. It is seen that the eigenfrequencies of the signal are not changed, but the first three anti-resonances are. Since λ contains the eigenfrequencies and damping values, the change of anti-resonance is accounted for by a change in the underlying mode shapes.

5.5 Modal fit

The last effort in the coupling of experimental data is by fitting the time response. A modal fit of the experimental data is necessary when interested in modal analysis or in our case; obtaining a clean set op impulse response functions for coupling purposes. Modal parameters are most commonly identified by curve fitting. Curve fitting is a process of matching a mathematical expression to a set of empirical data points. This is done by minimizing the squared error between the analytical function and the measured data[1]. The least squares complex exponential (lsce) method will be used. A description of this algorithm is given in appendix C [8].

The number of modes is over-specified to be 38, whereafter the computational modes are removed. The stabilisation diagram in figure C.1 shows that modal parameters up to 5 kHz can be distinguished. The poles represent the frequency and damping and the components of the mode shapes form the residue. When manually adding a rigid body mode (at zero Hertz), the impulse response function can be synthesised according to section 2.5.2 and is shown in figures 5.8a and 5.9a. It is clearly seen that the fitted response is cleaner in spectral representation, lacks the high frequency content and shows a transient exponential decay.

The impulse based substructuring scheme results in the coupled response and is shown in figures 5.8b and 5.9b. The impulse response shows that the period time is correctly estimated compared to that of the low-pass filtered measurement. Also the frequency response function shows the shift in harmonic frequencies compared to that of the substructure. Note that the there is a factor ten sampling frequency difference is this comparison.

[1] Note the similarities with the time-domain deconvolution operation.

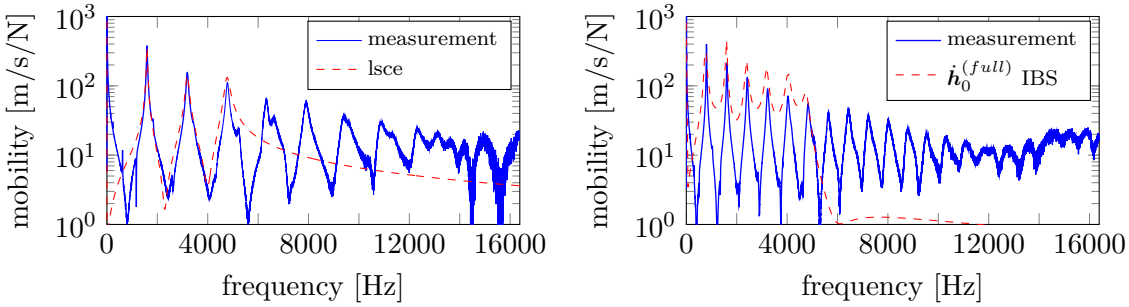

(a) *Measurement and lsce fit of subsystem* **(b)** *Measurement and IBS response of length 2L*

Figure 5.8: *FRF's of measurement, lsce fit and IBS coupled response.*

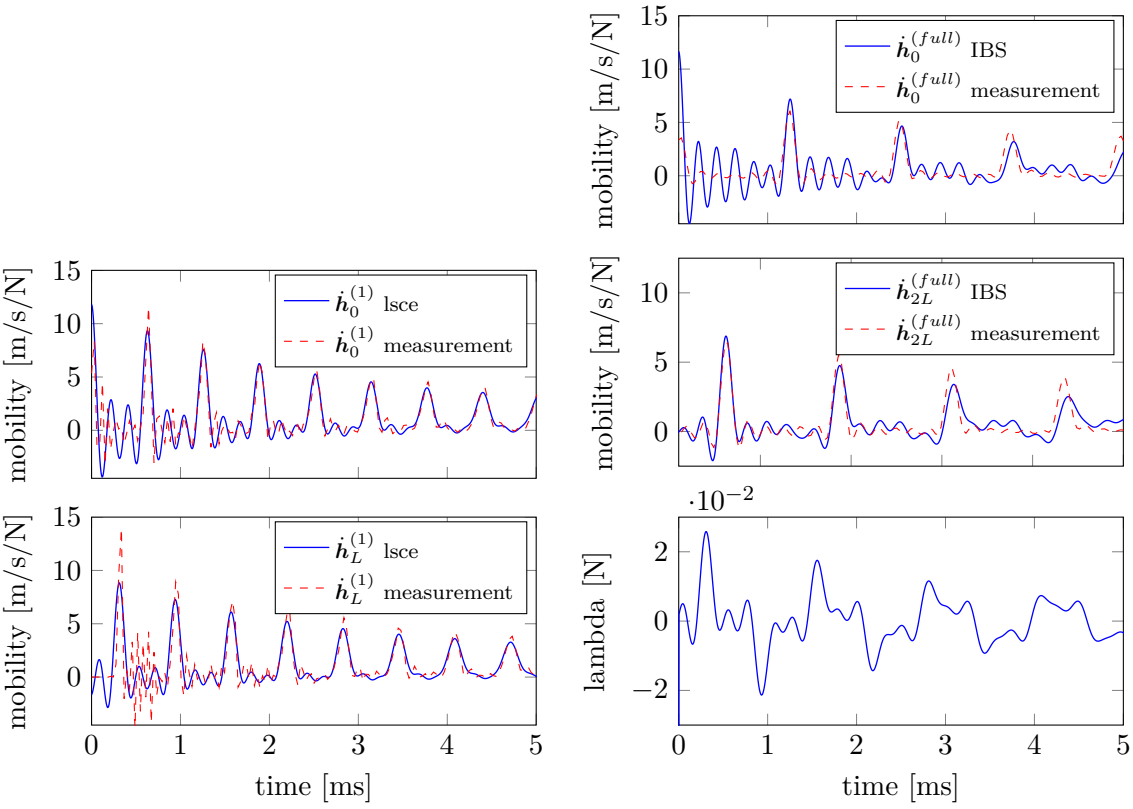

(a) *Modal fit of subsystem* **(b)** *Coupled full system responses*

Figure 5.9: *Modal fit of subsystems and the IBS coupled responses.*

5.6 Summary

The differences between the measurement and the simulated data were defined. In order to get rid of one of these differences, a quick solution of defining a hybrid impulse response was explored but did not achieve the desired coupled response. The experimental induced errors such as noise, different underlying dynamics and errors in the exponential decay were introduced on perfect numerical models to see their sensitivity to the impulse based substructuring scheme. The addition of noise and the changed underlying dynamics had no influence on the coupling process. A small amplitude error of the travelling waves resulted in decoupled results. This led to the identification of the modal parameters of the measurement to get rid of these amplitude errors, by means of the least squares complex exponential method. The acquired impulse response functions are, like the modal synthesised responses, perfectly usable in the impulse based substructuring scheme. The flowchart in figure 5.10 shows the processing steps necessary for experimental dynamics substructuring using impulse response functions and the additional subjects addressed in this chapter.

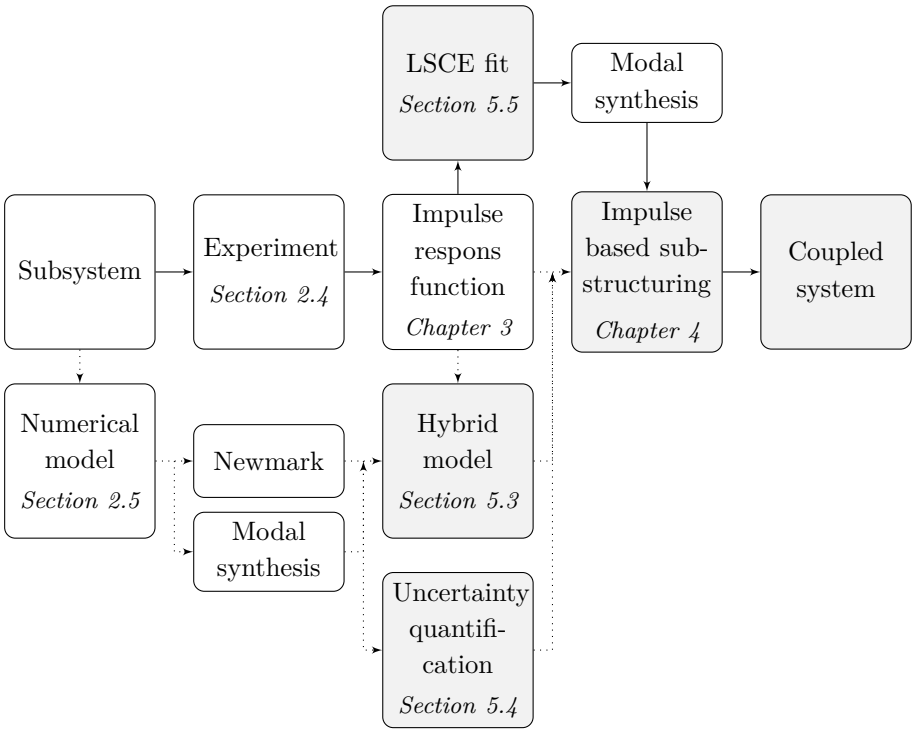

Figure 5.10: *Overview of subjects addressed in this chapter. The solid arrows give the processing steps necessary for dynamic substructuring with measured impulse response functions.*

Chapter 6

Conclusions and recommendations

6.1 Conclusions

In this work, a direct time-domain deconvolution operation has been developed and tested. This method is based on writing the Cauchy product in tensor form and the impulse response is found by solving a least-squares linear system. The formulation of the inverse FIR force filter, which is independent of the output response, allows for averaging between measurements and a high, low or bandpass filter can be built into the deconvolution operation. The latter is done by making use of the eigenvalues of the auto correlation matrix and formulating a pseudo inverse (section 3.4). The magnitude of the eigenvalues are similar to the auto power spectral density and can thus be used as a selection criteria between replicate measurements. The definition of the inverse filter is tested on three non perfect impacts to gain insight in its performance (section 3.6). It was found that the size of the Toeplitz matrix and the conditioning of the auto correlation matrix defines the accuracy and computational cost of the inverse filter. The inverse filter can also be defined by using a Fourier transform and its inverse. If both methods are compared, it is shown that the time-domain approach is less accurate and time efficient.

The equations of motion are solved by a Newmark time integration scheme and a modal synthesis. It was shown that the velocity can best be used for experimental dynamic substructuring purposes (section 2.5). The velocity is a superposition of delayed cosine functions and is less sensitive to trigger issues compared to the superposition of sine functions of the displacement and acceleration around $t = 0$. Another reason for abandoning the acceleration is the negative analytical value at time equal to zero, which leads to direct instability in the impulse based substructuring scheme.

The time integrated response functions can be used in the impulse based substructuring scheme independent of the size of the time step. The modally synthesised impulse response function can only be used for dynamic substructuring if the time steps are very small. The Newmark time integration scheme, which is consistent with the substructuring scheme, converges to the analytical solution for these small time steps. This makes coupling of modal synthesised impulse response functions very computationally demanding. The close correspondence of the measurement and the analytical solution, which are both down-sampled versions of the underlying continuum response, implies that the experimental data also needs a time step that is very small (section 4.3).

The direct time-domain deconvolution did not change the impulse response in such an extend that impulse based substructuring was possible (section 4.4). The observation of the differences between the measured and simulated data resulted in several test cases. A hybrid impulse response was constructed, sections of the measurement are replaced with simulated data, but did

not lead to a coupled stable response. The impulse based substructuring scheme is not sensitive to change of noise level, change in underlying dynamics and up-sampling of the analytical response. Note that this does not imply that a combination of these factors lead to a stable coupled response. The scheme is very sensitive to amplitude errors on the travelling waves. An amplitude error, a change in the exponential decay, less than one percent lead to decoupled full system responses (section 5.4.4).

The modal parameters of the measured impulse response functions are obtained by using the least squares complex exponential method, which operated in the time-domain. These modal parameters were utilised in synthesising a clean impulse response with a perfect exponential decay. The clean impulse response functions as the input for the impulse based substructuring scheme resulted in successful coupling (section 5.5).

6.2 Recommendations

Due to the fundamental nature of the exploratory research, not all the possible changes to the time measured impulse response were investigated in the effort of finding a coupled experimental response. Chapters 4 and 5 showed that dynamic substructuring with raw and slightly changed experimental impulse response functions was not possible. Fitting a pole-residue model on the empirical data made dynamic substructuring possible. The modal fit is a costly procedure and would ideally be avoided. The peaks of the travelling waves of the measurement could be scaled to a numerically obtained exponential decay, such the energy in the system is gradually reduced. Another change to the impulse response without fitting a model would be to compensate for the error in the output response, due to the non perfect impact, by the law of conservation of energy.

If the modal fit of the measured data stays necessary, the impulse based substructuring scheme is too expensive for the calculation of long time responses. Since it uses modal synthesised impulse response functions, the time step needs to approach zero to be consistent with the substructuring scheme. A substructuring scheme that is independent of the time step for modal synthesised response functions is very welcome.

6.2.1 Outlook

Next, the possibilities of the inverse filter will be discussed. Using the inverse filter is attractive when either the input or impulse response is known on forehand and the deconvolution operation needs to be performed in real-time. Another application would be to avoid the frequency domain effect of leakage.

Lightly damped structures are costly to test experimentally. The long vibration time makes testing and data storage expensive. The system must be completely damped out to obtain the most accurate frequency and damping parameters and avoid the frequency domain effect of leakage. The inverse force filter could change this procedure by deconvolving only the first part of the output response. Since the inverse filter is independent of the output response and operates in the time-domain, spectral leakage has no influence on the obtained impulse response. The truncation error, made by only taking a small section of the output response, is shown in figure D.1. A modal fit can be used on a short section of the impulse response for finding correct amplitude and phase parameters. These modal parameters are used for synthesising the complete impulse response.

The impulse response is known either from experimental testing or numerical modelling. This means that the inverse impulse response can be computed on forehand. If the output

response is measured in real-time, the inverse filter allows for obtaining the input response with a theoretical delay of the time step Δt. The truncation error of only using the first few periods is small, as graphically shown in figure D.1. This is done to keep the inverse filter of reasonable length.

A possible example for this application would be in the railway industry, where there is a need for the determination of different imperfections on the track. These imperfections introduce impact forces on the steel wheels of the train during motion. If the output response is measured in the bearings, the inverse impulse response could determine the impact force, if the system is assumed to behave linearly, in real time. With the known impact force, different imperfections can be quantified by examining the magnitude of its eigenvalues, i.e. the spectral content of the impact.

The input force is known in advance with a specific degree of certainty. The deconvolution operation, using the inverse filter, allows for the determination of the impulse response at a delay of the time step. The point wise availability of the impulse response can be used in the impulse based substructuring scheme, such that coupling in real time is possible (if the time step approaches zero).

Bibliography

[1] J.S. Bendat and A.G. Piersol. *Engineering applications of correlation and spectral analysis*. J. Wiley, 1993.

[2] M Bertero and P Boccacci. Introduction to inverse problems in imaging. *Bristol, Philadelphia*, 1998.

[3] S Butterworth. On the Theory of Filter Amplifiers. *Wireless Engineer*, 7, 1930.

[4] WH Kautz. Transient synthesis in the time domain. *Circuit Theory, Transactions of the IRE Professional Group on*, (3):29–39, 1954.

[5] D de Klerk, DJ Rixen, and SN Voormeeren. General framework for dynamic substructuring: history, review and classification of techniques. *AIAA journal*, 46(5):1169–1181, 2008.

[6] YW Lee, TP Cheatham Jr, and JB Wiesner. Application of correlation analysis to the detection of periodic signals in noise. *Proceedings of the IRE*, 38(10):1165–1171, 1950.

[7] L Lehmann. An effective finite element approach for soil-structure analysis in the time-domain. *Structural Engineering and Mechanics*, 21(4):437–450, 2005.

[8] N.M.M. Maia and J.M.M. Silva. *Theoretical and Experimental Modal Analysis*. Engineering dynamics series. Research Studies Press Limited, 1997.

[9] N.M. Newmark. A method of computation for structural dynamics. *Journal of the Engineering Mechanics Division of ASCE 85*, pages 67–94, 1959.

[10] Daniel J Rixen. A substructuring technique based on measured and computed impulse response functions of components. *ISMA*, 2010.

[11] Daniel J Rixen. Substructuring using impulse response functions for impact analysis. In *Structural Dynamics, Volume 3*, pages 637–646. Springer, 2011.

[12] Daniel J. Rixen and Paul L.C. van der Valk. An impulse based substructuring approach for impact analysis and load case simulations. *Journal of Sound and Vibration*, 332(26):7174 – 7190, 2013.

[13] P.L.C. Valk and D.J. Rixen. An Effective Method for Assembling Impulse Response Functions to Linear and Non-Linear Finite Element Models. In *Topics in Experimental Dynamics Substructuring and Wind Turbine Dynamics, Volume 2*, Conference Proceedings of the Society for Experimental Mechanics Series, pages 123–135. Springer New York, 2012.

[14] T. van der Horst and F. Wenneker. Experimental dynamic analysis on a high-end Aristides guitar. Technical report, Delft Unversity of Technology, special project: ME1460, May 2012.

[15] Maarten M.V. van der Seijs and Daniel J. Rixen. Efficient impulse based substructuring using truncated impulse response functions and mode superpositon. *Proceedings of ISMA 2012*, 2012.

[16] H. Wielandt. An extremum property of sums of eigenvalues. *Proceedings of the American Mathematical Society*, 6:106–110, 1955.

Appendix A

Inverse force filter

A.1 Implementation

```
function[h,time] = irf(f,u,N,dt)
% irf           Performes the deconvolution between the input f and output
%               u resulting in the impulse response h, for single
%               or multiple measurements.
%   [f]  Interval of the force function of interest, column matrix
%        [f1;f2;..] (windowed with lower and upper bound), M an odd number.
%   [u]  Output u starts at the lower bound of the force window,column
%        matrix [u1;u2,..].
%   [N]  An odd number specifying the accuracy of the inverse filter, scale
%        approx 4001 (depending on theconditioning of R).
%   [dt] Samping rate.
%

[M,b] = size(f);
Q     = N-M+1;
U     = numel(u(:,1));
% Correlation matrix
S = 2*M-1;                          % length auto-correlation vector
r = zeros(1,S);

for j = 1:b
    r = r + xcorr(f(:,j)).';        % (sum) auto-correlation vector
end

% Auto correlation matrix
R = sparse(N+M-1,Q);

for i=1:Q,
    R(i:((S+i-1)),i) = r;
end
O = (N+M-1-Q)/2;
R = R(O+1:N+M-1-O,:);

% Inverse force filter and convolution
f_inv = zeros(Q,b);
hhat  = zeros(U+Q-1,b);
for j= 1:b
frv = [zeros((Q-M)/2,1); flipud(f(:,j));zeros((Q-M)/2,1)];
f_inv(:,j) = R\frv;

```

```
41 % Impulse response
42 hhat(:,j) = conv(f_inv(:,j),u(:,j));
43 end
44
45 c = (N+1)/2;
46 if b>1
47     h = sum(hhat(c:c+U-M,:),2)/dt;
48 else
49     h = hhat(c:c+U-M)/dt;
50 end
51
52 time = 0:dt:(U-M)*dt;
53 end
```

A.2 Averaged comparison

Five repeated measurements are averaged. A perfect comparison if found, both in the amplitude and phase, see figure A.1.

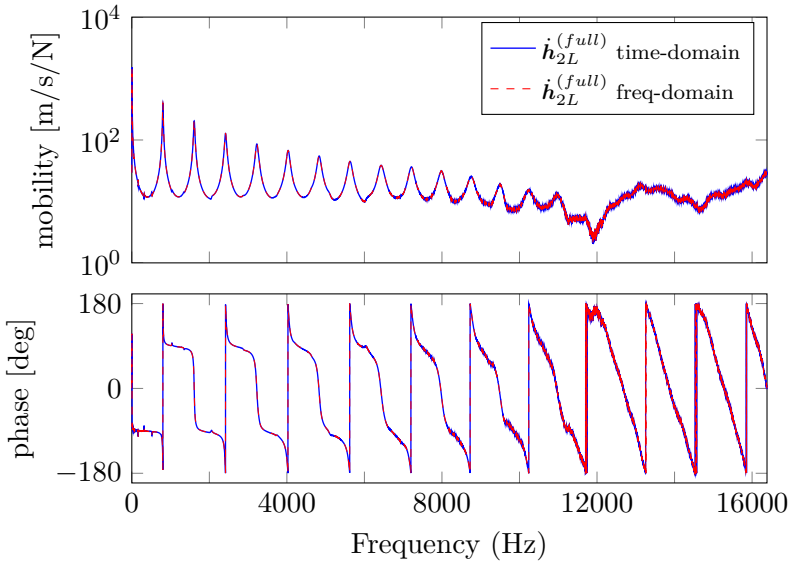

Figure A.1: *In blue the time-domain deconvolved impulse response function for 5 repeated measurements, in spectral representation. The red dashed line is the H_1 estimator, also for 5 measurements.*

Appendix B

Impulse based substructuring

The result of the IBS scheme for the impulse response functions at the end faces of the full bar. The sampling frequency of the analytical IRF's are equal to that of the measurement.

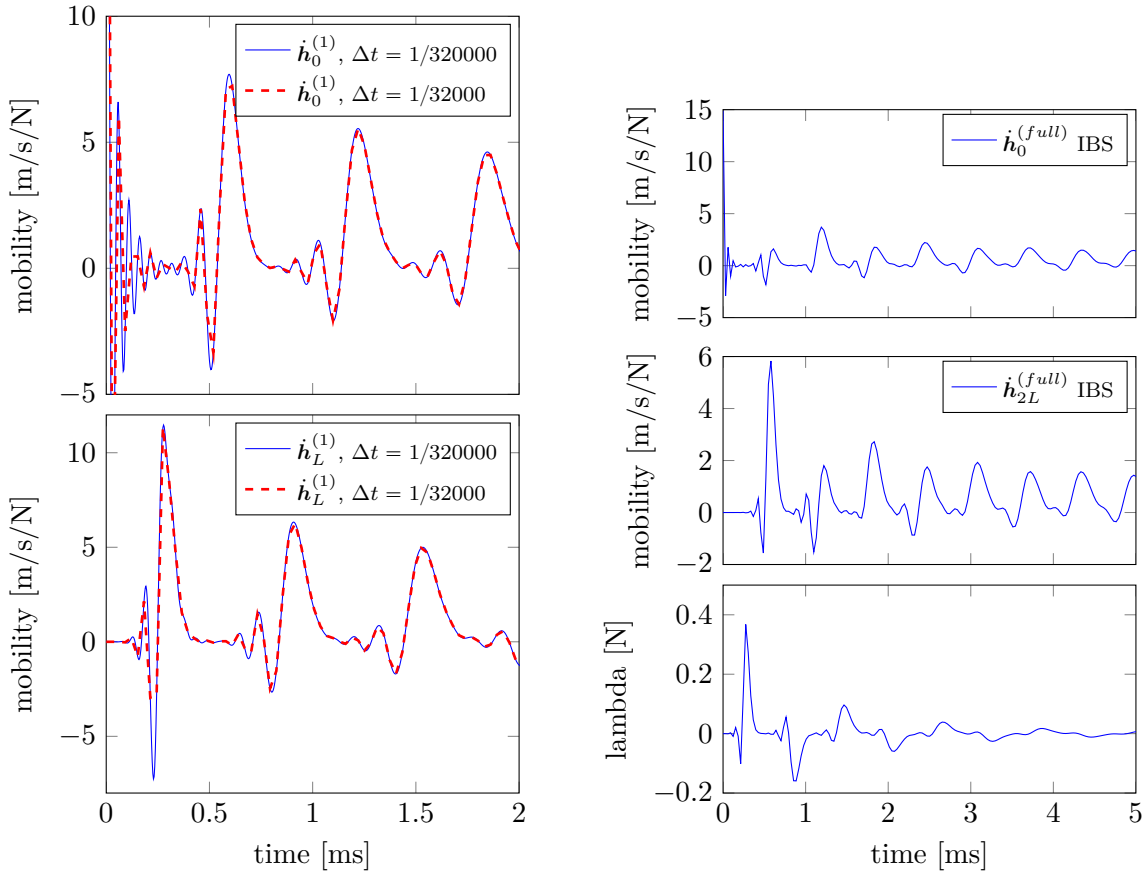

(a) *IRF's subcomponent for different sampling rates*

(b) *Modally synthesised IRF's show after IBS: a decoupled result*

Figure B.1: *Modally synthesised IRF's of the substructures for different sample frequencies. The result after IBS: an uncoupled response for the sample frequency of 1/32000*

Appendix C

Least-squares complex exponential

Different curve-fitting schemes are available for extracting modal parameters from experimental data. The least squares complex exponential method is chosen since is operates in the time domain. It calculates the system poles in the time domain by making use of the impulse response functions. When the system parameters are known, clean impulse response functions can be synthesised according to section 2.5.2. Assuming a constant sampling rate, equation (2.24) is rewritten in the form:

$$\boldsymbol{h}(m\Delta t) = 2Re\left(\sum_{j=1}^{n} \boldsymbol{R}_j V_j^m\right) \tag{C.1}$$

The abbreviation $V_j = e^{\lambda_j \Delta t}$ is used. Note that the values of $\boldsymbol{R}_j$ and V_j are not known. For the solution, Prony's method is used. Because the roots for a non-critically damped systems always occur in complex conjugate pairs, so does the abbreviation V_j. Auto regressive moving average models are introduced to solve the polynomial of order L with real coefficients β:

$$\beta_0 + \beta_1 V_j + \beta_2 V_j^2 + \ldots + \beta_L V_j^L = 0 \tag{C.2}$$

First the values of β_p are solved with the following overdetermined system of equations, in the same least squares manner as seen in chapter 3, by assuming $\beta_L = 0$

$$\sum_{p=0}^{L} \beta_p \boldsymbol{h}(m\Delta t) = 0 \tag{C.3}$$

Then, V_j follows from the polynomial roots of equation (C.2). The abbreviation of the exponential function helps in finding the system poles:

$$\lambda_j = \frac{1}{\Delta t}(\ln|V_j| \pm i \arg(V_k)) \tag{C.4}$$

This procedure can be expanded to a single input multiple output method by increasing the overdetermined system of equation (C.3) in a similar way as the time domain averaging. In the averaging case was the impulse response independent of the replicate output measurements and here are the constants β independent of the number of impulse responses.

C.1 Stabilisation diagram

The stabilisation diagram in figure C.1 shows the result of the least-squared complex exponential fit. It was used for determining the modal parameters of the experimental obtained IRF's of the subcomponents.

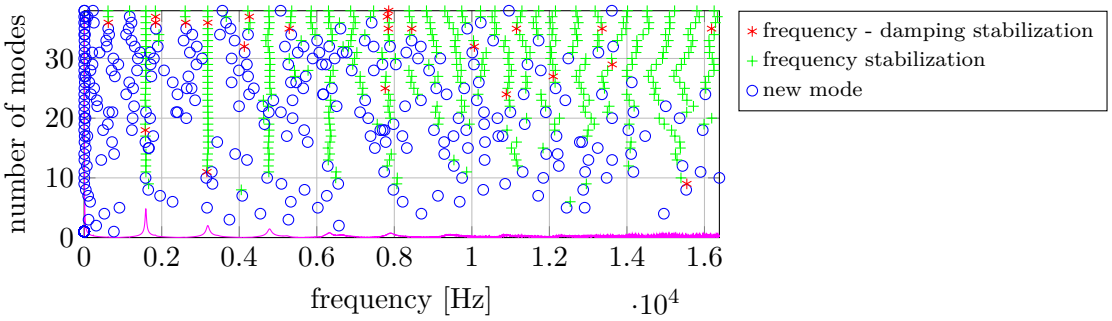

Figure C.1: *LSCE stabilisation diagram of subsystem measurements.*

Appendix D

Response truncation

Since the inverse FIR force filter is independent of the output response, the output can be truncated in the time domain without any effects of leakage. The truncated versions of the impulse response are transferred to the frequency domain (leakage has effect on the displayed results and the frequency resolution is significantly different since no zeros are added). The results are shown in figure D.1. The reference impulse response has $n_{max} = 32.8 \times 10^3$ samples. The truncation at t_1 uses $0.06n_{max}$, t_2 uses $0.065n_{max}$, t_3 uses $0.08n_{max}$ and t_4 uses $0.11n_{max}$ samples.

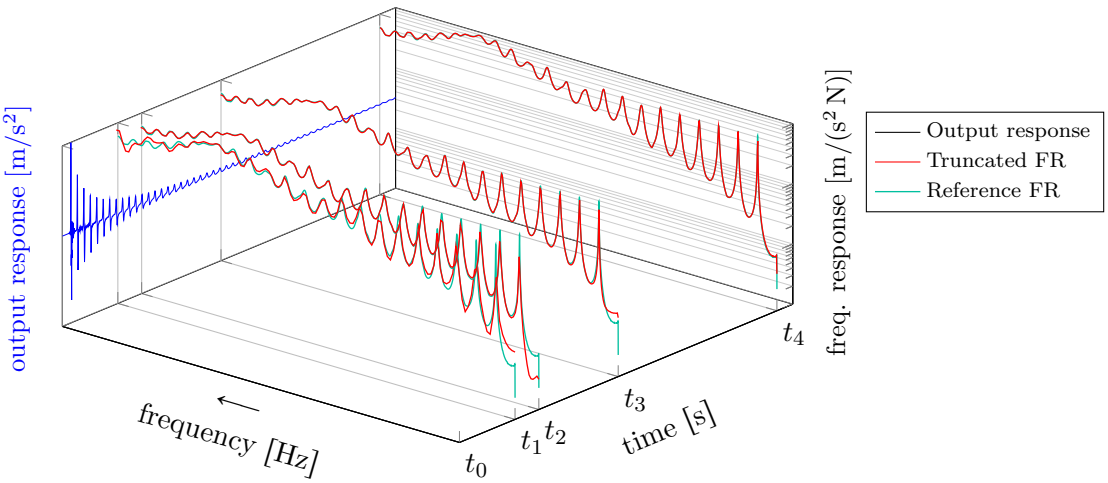

Figure D.1: *The impulse response obtained from convolving the inverse filter with the truncated versions of the output response is converted to the frequency domain and compared to the reference frequency response, found with the full length output response (t_max).*


TU Delft
Delft
University of
Technology